Washington University in St. Louis
Washington University Open Scholarship

All Theses and Dissertations (ETDs)

Summer 8-1-2013

Numerical Simulation of Separated and Secondary Flows in Diffusing S-Ducts for Air Breathing Propulsion

Colin James Fiola
Washington University in St. Louis

Follow this and additional works at: https://openscholarship.wustl.edu/etd

 Part of the Mechanical Engineering Commons

Recommended Citation

Fiola, Colin James, "Numerical Simulation of Separated and Secondary Flows in Diffusing S-Ducts for Air Breathing Propulsion" (2013). *All Theses and Dissertations (ETDs)*. 1168.
https://openscholarship.wustl.edu/etd/1168

This Thesis is brought to you for free and open access by Washington University Open Scholarship. It has been accepted for inclusion in All Theses and Dissertations (ETDs) by an authorized administrator of Washington University Open Scholarship. For more information, please contact digital@wumail.wustl.edu.

WASHINGTON UNIVERSITY IN ST. LOUIS
School of Engineering and Applied Science
Department of Mechanical Engineering and Material Science

Thesis Examination Committee

Dr. Ramesh K. Agarwal (Chair)

Dr. David A. Peters

Dr. Kenneth Jerina

Numerical Simulation of Separated and Secondary Flows in Diffusing S-Ducts for Air Breathing Propulsion

by

Colin J. Fiola

A thesis presented to the School of Engineering and Applied Science
of Washington University in partial fulfillment of the
requirements for the degree of
Master of Science

August 2013

Saint Louis, Missouri

Contents

List of Figures

List of Abbreviations

S-duct – Serpentine Duct

UAV – Unmanned Aerial Vehicle

RANS – Reynolds-Averaged-Navier-Stokes-Equations

SA – Spallart-Allmaras

NASA – National Aeronautics and Space Administration

CFD – Computational Fluid Dynamics

AIAA – American Institute of Aeronautics and Astronautics

PAW – Propulsion Aerodynamics Workshop

ONERA – Office National d'Études et de Recherches Aérospatiales

AIP – Aerodynamic Interface Plane

UDF – User Defined Function

Acknowledgments

First, and foremost, I would like to thank Professor Ramesh K. Agarwal for believing in my talents, staying patient through my struggles, and being a stalwart leader of my research pursuits. I would also like to thank the Missouri Space Grant Consortium for providing funding for this intellectual pursuit.

I would also like to thank my parents for their continuous support of my academic ventures. My wife, Erika, deserves many thanks as she dealt with my long hours in the CFD laboratory and sometimes with my grumpy mood upon my arrival home.

Colin J. Fiola

Washington University in St. Louis
August 2013

ABSTRACT OF THE THESIS

Numerical Simulation of Separated and Secondary Flows in Diffusing S-Ducts

for Air Breathing Propulsion

by

Colin J. Fiola

Master of Science in Aerospace Engineering

Washington University in St. Louis, August 2013

Research Advisor: Professor Ramesh K. Agarwal

The focus of this thesis is on numerical simulation of incompressible and compressible flow in a diffusing S-duct inlet. S-ducts are very common components of both commercial and military aircraft, for example the Boeing 727 and McDonnell Douglas F-18. The F-18, being a relatively small aircraft, requires a short, highly curved S-duct with non-uniform cross-sectional area. The S-duct decelerates the flow, increasing the static pressure, in order to provide a uniform velocity and pressure distribution at the engine face. The curved nature and increasing cross sectional area creates secondary flows and boundary layer separation which causes non-uniform flow and total pressure loss at the engine face. Total pressure loss and flow non-uniformity at the engine face reduce engine performance and cause increased wear on parts such as turbine blades. Engine stall is also a concern when the flow inside the S-Duct becomes highly distorted. An ideal S-duct would efficiently decelerate flow uniformly while minimizing total pressure loss and magnitude of transverse velocity components. Due to the necessity to minimize size and maximize stealth of aircraft, including Unmanned Aerial Vehicles (UAVs) and cruise missiles, designers are challenged to use shorter and

more highly curved S-Ducts. The accurate modeling of flow in S-duct is therefore a problem of great interest and significance in propulsion. In this thesis, we study the flow field in S-ducts by numerical simulations using the Reynolds-Averaged Navier-Stokes (RANS) equations in conjunction with a variety of one – and two equation turbulence models such as one-equation Spalart-Allmaras model, the two-equation k-ε and SST k-ω models, and the four equations Transition SST model. Two S-duct geometries are employed in this investigation – one is used in an experimental study conducted at NASA Glenn Research Center in the early 1990's, the other is a benchmark configuration proposed by AIAA Propulsion Aerodynamics Workshop to assess the accuracy and best practices of CFD solvers. The CFD flow solver ANSYS-FLUENT is employed for computing the incompressible/compressible flow inside the S-ducts. A structured mesh is generated using GAMBIT. A second-order accurate steady density-based solver is employed in a finite-volume framework. The computed results compare well with the experimental data and with the computations of other investigators. The flow field and pressure recovery are captured with good accuracy. The best practices for CFD modeling, namely the mesh density, the accuracy of the algorithm and the turbulence model, of S-duct flow field are identified.

Chapter 1

Introduction

This chapter provides the background of the S-duct and the motivation behind the study of S-duct flow fields. Two geometric configurations of S-ducts to be studied are described.

1.1 Motivation and Goals

Computational Fluid Dynamics (CFD) is routinely used in the aerospace industry as an analysis tool to test and validate the design of systems and components involving fluid flow. The aircraft components may include wings, fuselages, tails etc. and engine components may include inlets, compressors, turbines, combustors and nozzles. However the accuracy of CFD solutions still remains a matter of concern because it depends upon the accuracy of the algorithm, the density and quality of the mesh, and the turbulence model employed. Therefore, there is a need for establishing best practice guidelines for CFD analysis so that the CFD solutions can be used with some confidence in the analysis and design of aerospace components and systems. Several of these configurations inherently have highly three-dimensional fluid flows which can give rise to very complex flow phenomena posing a challenge for CFD software to accurately predict these flow fields. The Serpentine Diffuser (S-duct) is one such configuration.

S-ducts are a very common component of both commercial and military aircraft, for example the Lockheed Martin L-1011, Boeing 727 and McDonnell Douglas F-18 [1]. The F-18, being a relatively small aircraft, requires a short, highly curved S-duct with non-uniform cross-sectional area. S-duct joins an externally mounted inlet to an internally (within the fuselage) mounted engine, providing necessary air for combustion.

Figure 1.1 illustrates the use of an S-Duct for an inlet of an internally mounted jet engine in the Lockheed Martin L-1011 aircraft [2].

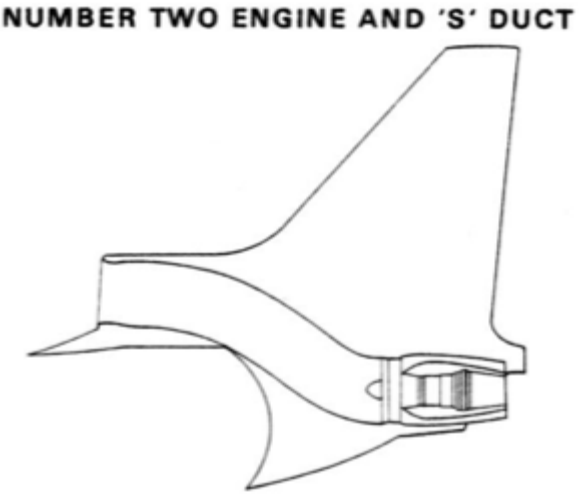

Figure1.1 S-Duct in tail section for jet engine in Lockheed L-1011 [2]

The flow inside the S-duct is characterized by boundary layer separation and secondary flow, as was found in the experiments conducted at NASA Glenn Research Center in 1990's [3]. A diffusing S-Duct, as used in the NASA Glenn experiment, is characterized by not only centerline curvature, but also an increase in radius along the centerline. The S-duct decelerates the flow, increasing the static pressure, in order to provide a uniform velocity and pressure distribution at the engine face [4]. The curved nature and increasing cross sectional area creates secondary flows and boundary layer separation which causes non-uniform flow and total pressure loss at the engine face. Total pressure loss and flow non-uniformity at the engine face reduce engine performance and cause increased wear on parts such as turbine blades [5]. Engine stall is also a concern when the flow inside the S-Duct becomes highly distorted. An ideal S-duct would efficiently decelerate the flow while minimizing the total pressure loss and reducing the magnitude of transverse velocity components [3].

Due to the necessity to minimize size and maximize stealth of aircraft, including Unmanned Air Vehicles (UAVs) and cruise missiles, designers are challenged to use

shorter and more highly curved S-Ducts [4, 5]. Shortening an S-Duct causes larger increase in centerline curvature and adverse pressure gradients thus leading to the possibility of diminished performance [1]. S-Ducts maximize the stealth characteristics of an aircraft by hiding the spinning turbine blades which reflect radar. The accurate modeling of flow in S-duct is therefore a problem of great interest and significance in propulsion and aircraft design aerodynamics. In recent years, there has also been emphasis on both passive and active flow control devices to modify the flow inside the S-duct to reduce separation and enhance pressure recovery [6].

The goal of this research is to perform numerical simulations for two S-duct configurations and compare them with the available experimental data. These two configurations are: (1) employed in NASA Glenn Research Center's experimental study [3] and (2) the CFD validation case proposed in the American Institute for Aeronautics and Astronautics' Propulsion Aerodynamics Workshop (AIAA PAW) [7].

1.2 NASA Glenn Research Center's S-Duct Geometry

The experimental NASA Glenn S-duct was designed to study the complex three-dimensional turbulent flow phenomena such as the boundary layer separation and secondary flows [3]. The duct's centerline was created by the union of two identical circular arcs, both of the same radius R = 1.02m, and located in the same plane. Equations 1.1 – 1.3 below are used to create the centerline of the duct, where $\frac{\theta_m}{2} = 30^o$.

$$x_{cl} = \begin{cases} R\sin\theta\,, & 0 \le \theta \le \frac{\theta_m}{2} \\ 2R\sin\left(\frac{\theta_m}{2}\right) - R\sin(\theta_m - \theta)\,, & \frac{\theta_m}{2} \le \theta \le \theta_m \end{cases} \tag{1.1}$$

$$y_{cl} = 0 \tag{1.2}$$

$$z_{cl} = \begin{cases} R\cos\theta - R, \ 0 \le \theta \le \frac{\theta_m}{2} \\ 2R\cos\left(\frac{\theta_m}{2}\right) - R(1+\cos(\theta_m - \theta)\,, \ \frac{\theta_m}{2} \le \theta \le \theta_m \end{cases} \tag{1.3}$$

The duct's area diffuses along the centerline, which is the radius r increases along centerline given by Equation 1.4 below.

$$\frac{r}{r_1} = 1 + 3\left(\frac{r_2}{r_1} - 1\right)\left(\frac{\theta}{\theta_m}\right)^2 - 2\left(\frac{r_2}{r_1} - 1\right)\left(\frac{\theta}{\theta_m}\right)^3 \tag{1.4}$$

The area ratio of the S-duct (ratio between the outlet and inlet cross sectional area) is equal to 1.52. The inlet diameter, r_1, is 0.1021 m and the outlet diameter, r_2, is 0.1257 m. The offset of the intake resulting from the centerline curvature is 1.34 times the inlet diameter, D_1. Figure 1.2 shows the duct's geometry as well as angles and radii used for the creation of centerline.

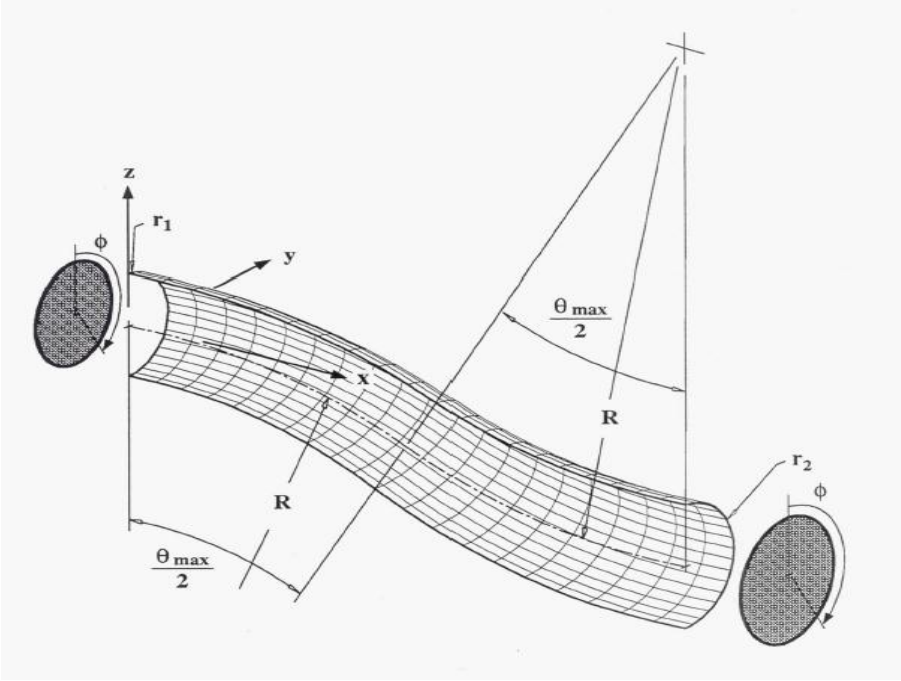

Figure 1.2 NASA Glenn S-Duct Geometry [3]

1.3 AIAA Propulsion Aerodynamics Workshop Test Case S-Duct Geometry

The AIAA Propulsion Aerodynamics Workshop (PAW) S-Duct geometry [7] is similar to that of the NASA Glenn Research Center's geometry, Figure 1.2 [3] except that it is scaled to fit an experimental sonic throat mass flow meter. The Office National d'Études et de Recherches Aérospatiales (ONERA) in France, has created this geometry to produce the experimental sonic throat mass flow meter which is called '40 Kulite rake.' The S-duct inlet is joined by a straight portion of constant diameter duct with a bell-mouth inlet. The S-duct outlet is joined by non-uniform area duct which houses a mass flow plug. Figures 1.3 and 1.4 respectively provide a schematic and actual view of the S-duct and the test apparatus employed in the ONERA experiment.

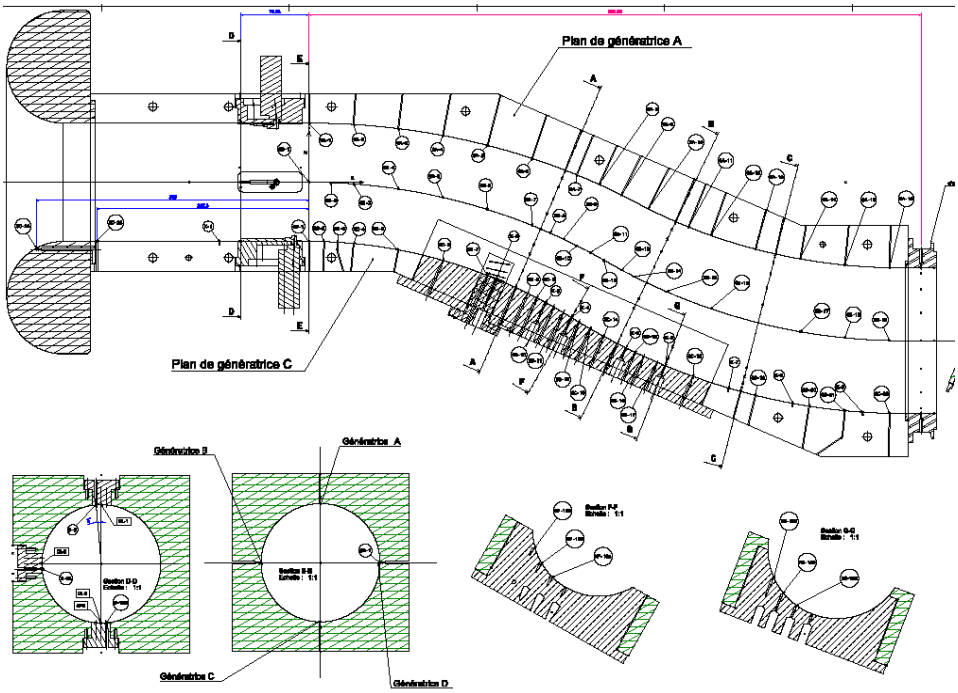

Figure1.3 AIAA PAW S-Duct configuration [7]

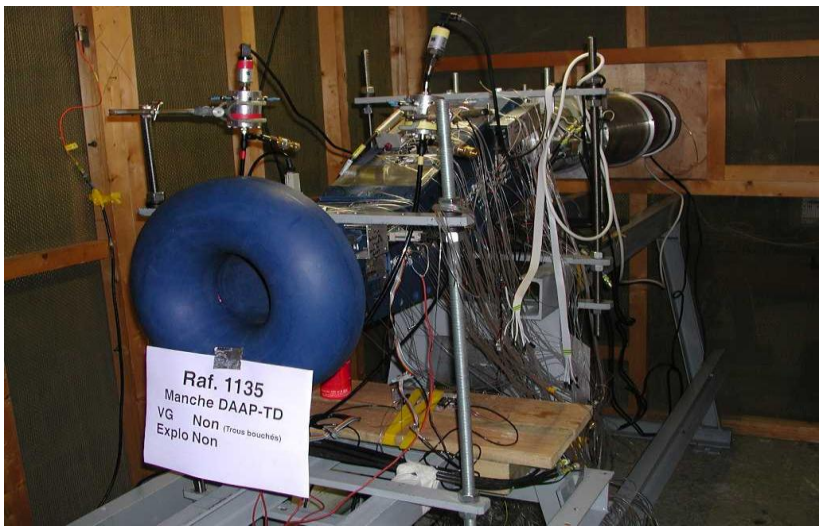

Figure1.4 AIAA PAW S-Duct (ONERA) experimental apparatus [7]

Similar to the NASA Glenn Research Center's S-duct [3], the area ratio between the inlet and outlet of the ONERA S-duct is 1.52. The inlet diameter D_1 is 0.13315 m and the outlet diameter D2 is 0.164 m, which matches the diameter of the experimental '40 Kulite rake.' The '40 Kulite rake' has eight equally spaced arms each with five Pitot pressure probes to measure stream-wise pressure, as shown in Figure 1.5. Along the walls of the duct are four rows of static pressure taps at ϕ = 0°, 90º, 180°, and 270º.

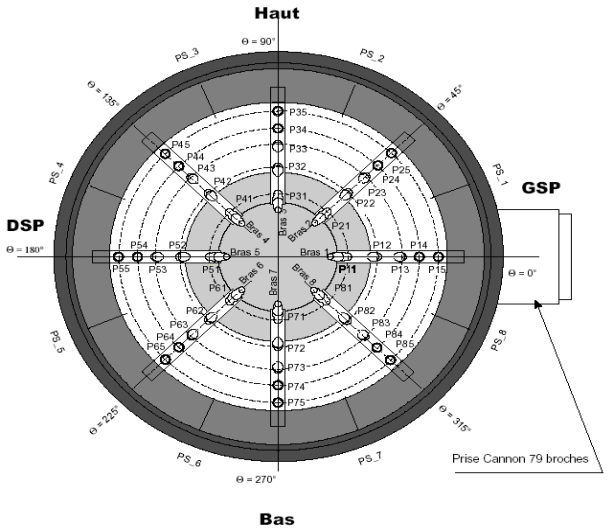

Figure 1.5 ONERA '40 Kulite' dynamic rake

Chapter 2

Elements of Numerical Analysis

The necessary preparation for numerical analysis is presented in this chapter. This preparation includes mesh generation, flow solver considerations, and development of boundary conditions.

2.1 Mesh Generation

The software used to create the mesh for both S-duct configurations employed in study is ANSYS ICEM CFD [8]. This software provides the user with a high quality multi-block hexahedral volume mesh. All meshes created are of high quality and high density to capture the geometry and the flow field quite well.

2.1.1 NASA Lewis Research Center S-Duct Mesh

The geometry of the NASA Glenn Research Center S-Duct was constructed in ANSYS ICEM CFD using Equations 1.1-1.4 for geometry. The half-model was considered for computational efficiency since the flow is symmetric [3]. Constant diameter ducts of length $3.75D_1$ were attached at the inlet and outlet of the S-Duct in order to provide smooth and uniform flow at entrance and exit. The computational domain is shown in Figure 2.1.

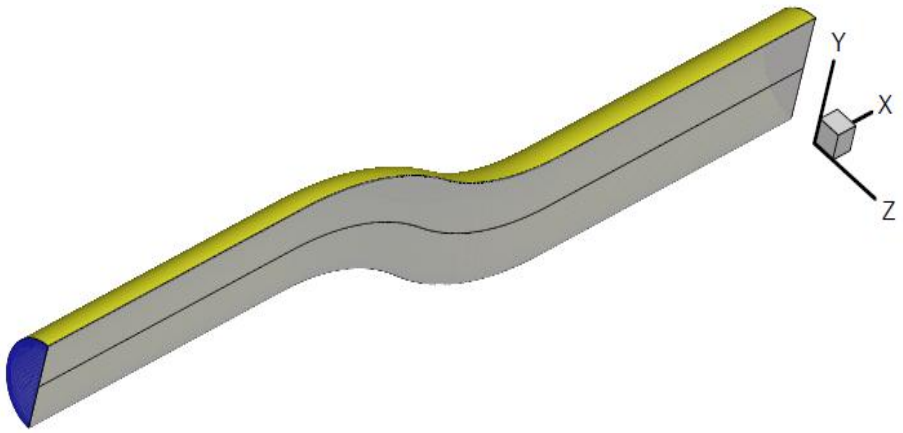

Figure 2.1 NASA Glenn S-Duct computational domain

An O+H block grid structure was used to accurately capture the curvature of the duct. The O+H block grid structure also allows for a very fine near-wall mesh in order to accurately capture the viscous boundary layer, it is shown in Figure 2.2. The y+ value for the first point off the wall surface is nearly one. The mesh consists of 3,592,752 hexahedral cells.

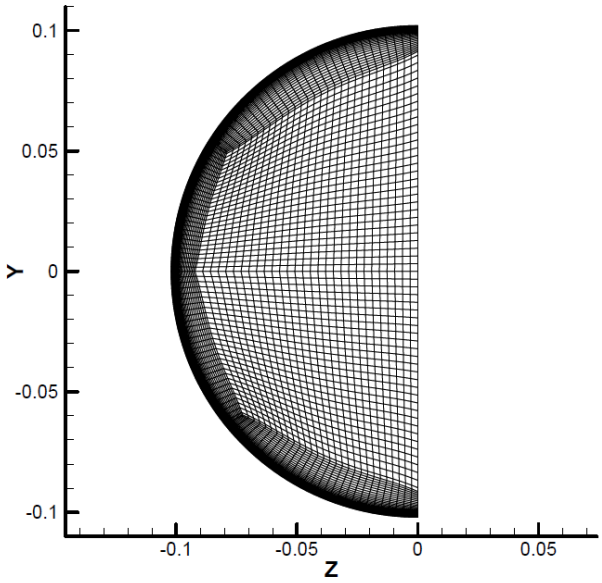

Figure 2.2 NASA Glenn S-Duct cross-section view of the mesh at inlet of S-duct demonstrating the O+H block grid structure.

2.1.2 AIAA Propulsion Aerodynamics Workshop S-Duct Mesh

The AIAA Propulsion Aerodynamics Workshop (PAW) S-Duct's geometry was provided by ONERA. The mesh was generated in a similar fashion as for the NASA Glenn case using the ANSYS ICEM CFD. The computational domain of the AIAA Propulsion Aerodynamics Workshop S-Duct is shown in Figure 2.3.

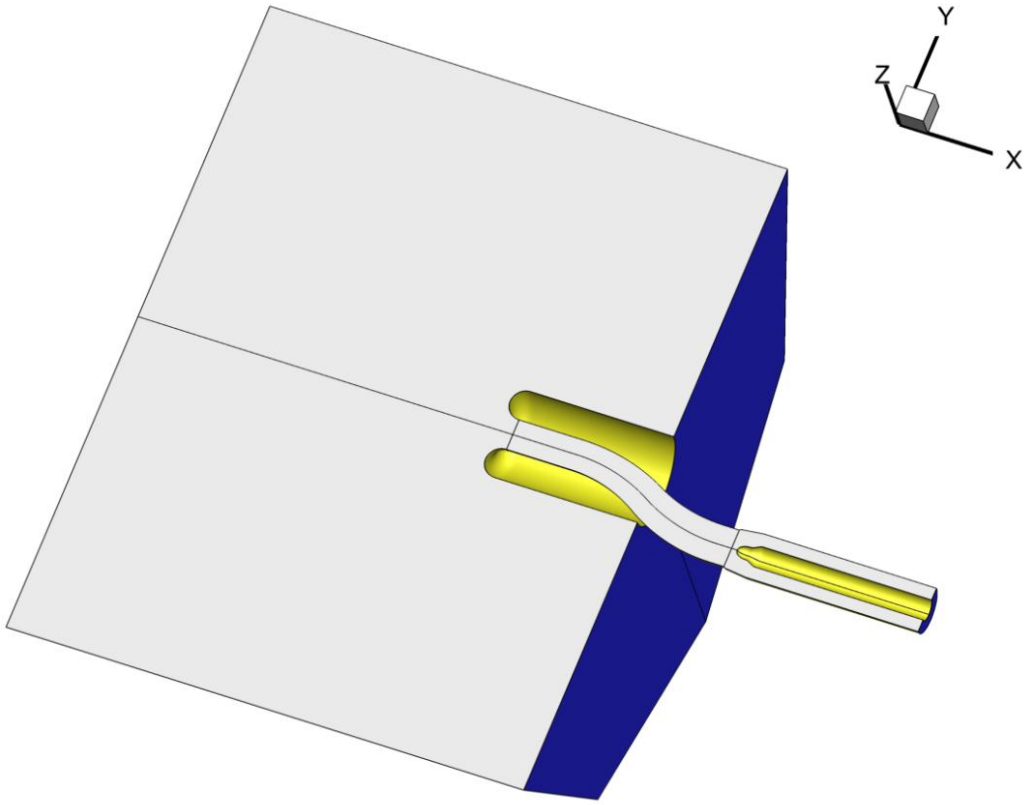

Figure 2.3 AIAA PAW S-duct computational domain

The block grid structure in the duct remains O+H, but varies near the duct inlet and exit. Figure 2.4 shows the O+H grid structure in the AIAA PAW S-Duct. The variation in block grid structure near the inlet is needed due to complex bell-mouth inlet and it is needed near the exit due to mass flow plug. The y+ value for the first point off the wall

surface is nearly one to ensure accurate viscous boundary layer resolution in the simulations. The mesh consists of 7,690,475 hexahedral cells.

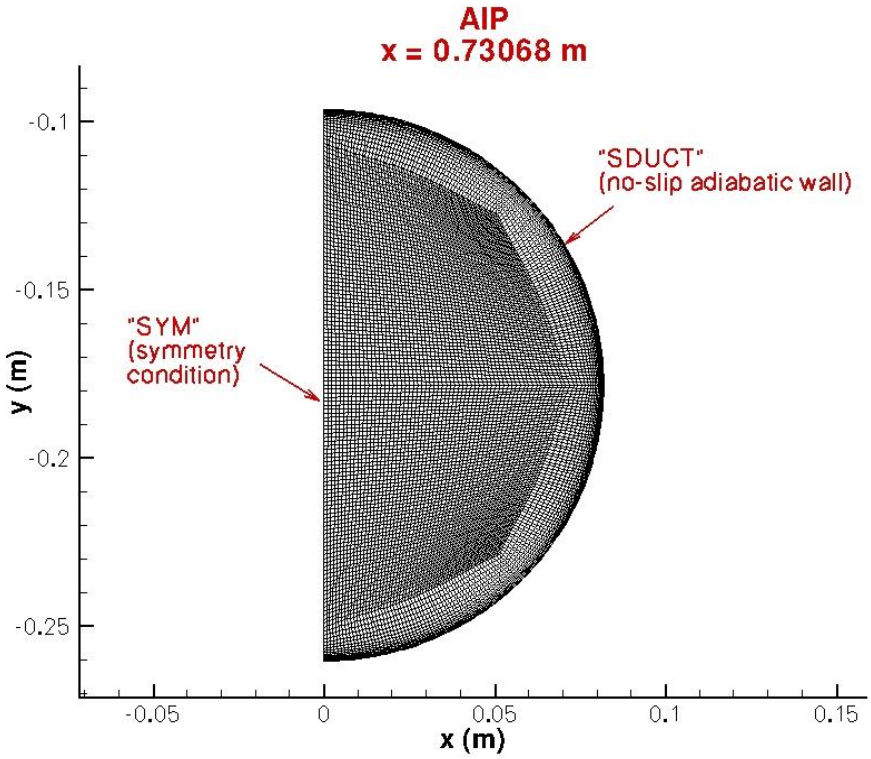

Figure 2.4 AIAA PAW O+H block grid structure at the Aerodynamic Interface Plane (AIP) [7]

2.2 Boundary Conditions

Boundary conditions were applied in both the simulation cases to match the experimental conditions. Both cases relied primarily on outflow conditions in order to match Mach number in selected analysis planes: the reference inlet and Aerodynamic Interface Plane (AIP).

2.2.1 NASA Glenn Research Center S-Duct Boundary Conditions

Boundary conditions were assigned in order to match the NASA Glenn experiment's flow conditions [3]. The inlet was assigned as a 'pressure inlet' whose total pressure and total temperature matched the experimental flow conditions of the specified inlet Mach number. The walls were assigned as 'solid walls' which were stationary with no-slip adiabatic condition. The outlet was set as 'mass flow inlet' with an outward normal flow direction vector. The mass flow rate of the outlet was set so as to match the prescribed centerline Mach number of M = 0.6 at the reference inlet. The symmetry boundary condition was applied in the 'symmetry plane'. This symmetry condition is valid because the flow has been experimentally proven symmetric [3].

2.2.2 AIAA Propulsion Aerodynamics Workshop S-Duct Boundary Conditions

Boundary conditions were assigned to match those provided by AIAA PAW [7]. The 'far field' inlet was assigned as 'pressure inlet' at atmospheric conditions. The walls were assigned as 'solid wall' which were stationary with no-slip adiabatic condition. The outlet was set as 'mass flow inlet' with an outward normal flow direction vector. The mass flow was set at 1.2135 kg/s for the half model with a total pressure of 88,744 Pa and total temperature of 286.2 K, as given by AIAA PAW. Much like the NASA Lewis S-duct, the symmetry boundary condition was assigned to the 'symmetry plane.' Figure 2.5 and 2.6 respectively show the AIAA PAW S-Duct geometry and the boundary conditions associated with the computational domain.

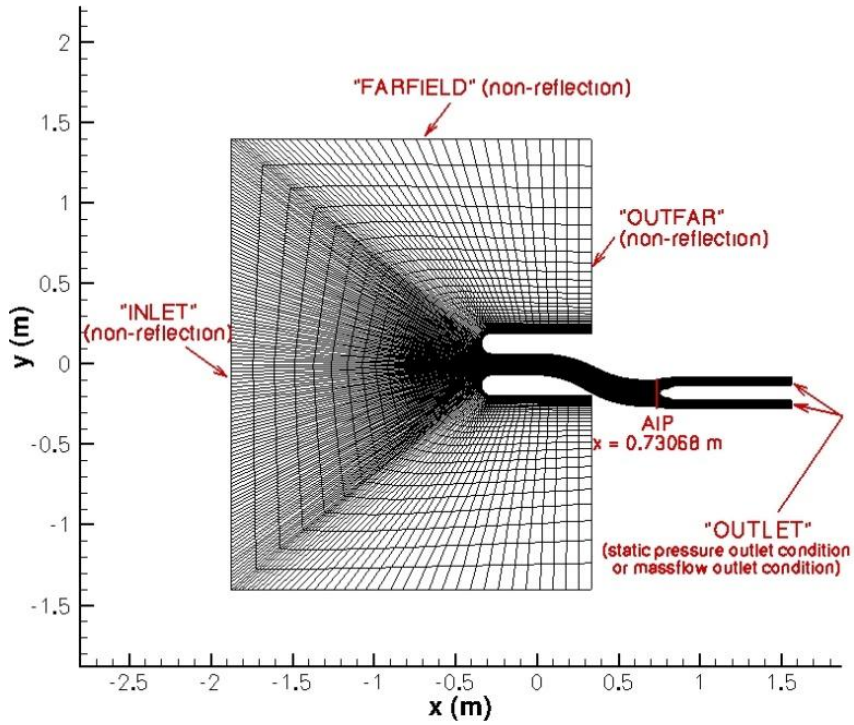

Figure 2.5 AIAA PAW computational domain with boundary conditions [7]

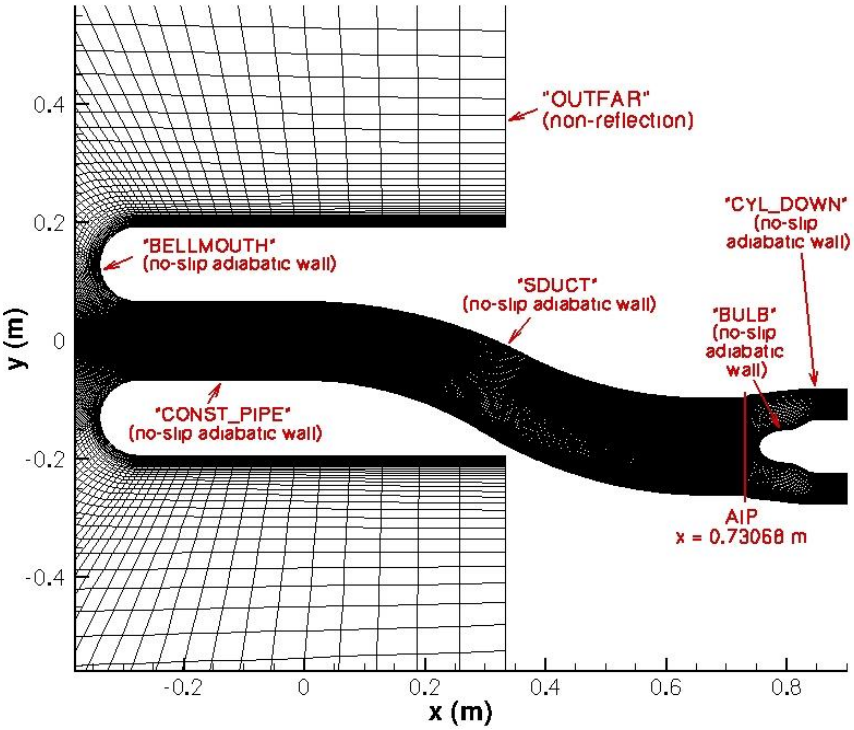

Figure 2.6 AIAA PAW S-duct section (zoomed-in view) with boundary conditions [7]

2.3 CFD Flow Solver

The CFD flow solver used is ANSYS Fluent [9]. Fluent is a commercial solver which solves three-dimensional Reynolds-Averaged-Navier-Stokes (RANS) equations on structured and/or unstructured meshes. The solver employed in the simulations is steady and able to analyze both the compressible and incompressible flows in the S-duct. Fluent provides a number of turbulence models, namely the one-equation Spalart-Allmaras (SA) model, the two equation k-ϵ and k-ω SST models and the four equation Transition SST model. Fluent also has the capability to run on parallel Graphical Processing Units (GPUs) which can greatly speed up the calculations.

2.3.1 Turbulence Modeling

A number of turbulence models were used to investigate the NASA Glenn Research Center S-Duct configuration. Four turbulent models were selected: the one-equation Spalart-Allmaras (SA) model, the two equation k-ϵ and k-ω SST models and the four equation Transition SST model. The complexity of the turbulence model decreases the efficiency and increases the cost of simulation.

The first turbulence model studied was the Spalart-Allmaras (SA) model which is a single transport equation model. The next two models employed were the two-equation k-ε and k-ω models. The standard *k-ε* model is modified with a near-wall treatment to improve the accuracy in the wall region in adverse pressure gradient flow resulting in separation. Two equation Shear Stress Transport (SST) k-ω model was also used to evaluate its accuracy for computing separated and secondary flow. Finally, the four equation Transition SST model was employed to see if there were transitional effects in the flow.

Chapter 3

Numerical Simulation Procedure

The numerical solution procedure by which each S-Duct case is analyzed is presented in this chapter. The two cases are analyzed using the non-dimensional quantities whose equations and formulations are presented.

3.1 Geometric Considerations

In order to best match the experimental results obtained by the NASA Glenn Research Center for their S-duct [3], some geometric and non-dimensionality considerations for the variables must be made in presenting the results of numerical simulation. The experimental results are presented in non-dimensional coordinates and non-dimensional flow variables. When referring to the position of a particular cross-section of the duct, the ratio of centerline distance from the inlet (s) to the inlet diameter (D_1) is used. Thus, the location of S-duct's geometric inlet corresponds to $s/D_1=0$, which also corresponds to the physical coordinate of x = 0m. The S-Duct's geometric outlet corresponds to $s/D_1=5.23$.

Multiple cross-sectional planes are used in comparing the experimental and computational results as shown in Figure 3.1. Of these planes, two are of special interest. The first plane is the reference inlet plane, which is located one radius upstream of the geometric inlet at s/D1 = -0.5 (Plane A in Figure 3.1). The second plane is the

Aerodynamic Interface Plane (AIP). The AIP is located one radius after the geometric outlet at s/D1=5.73 (Plane E in Figure 3.1).

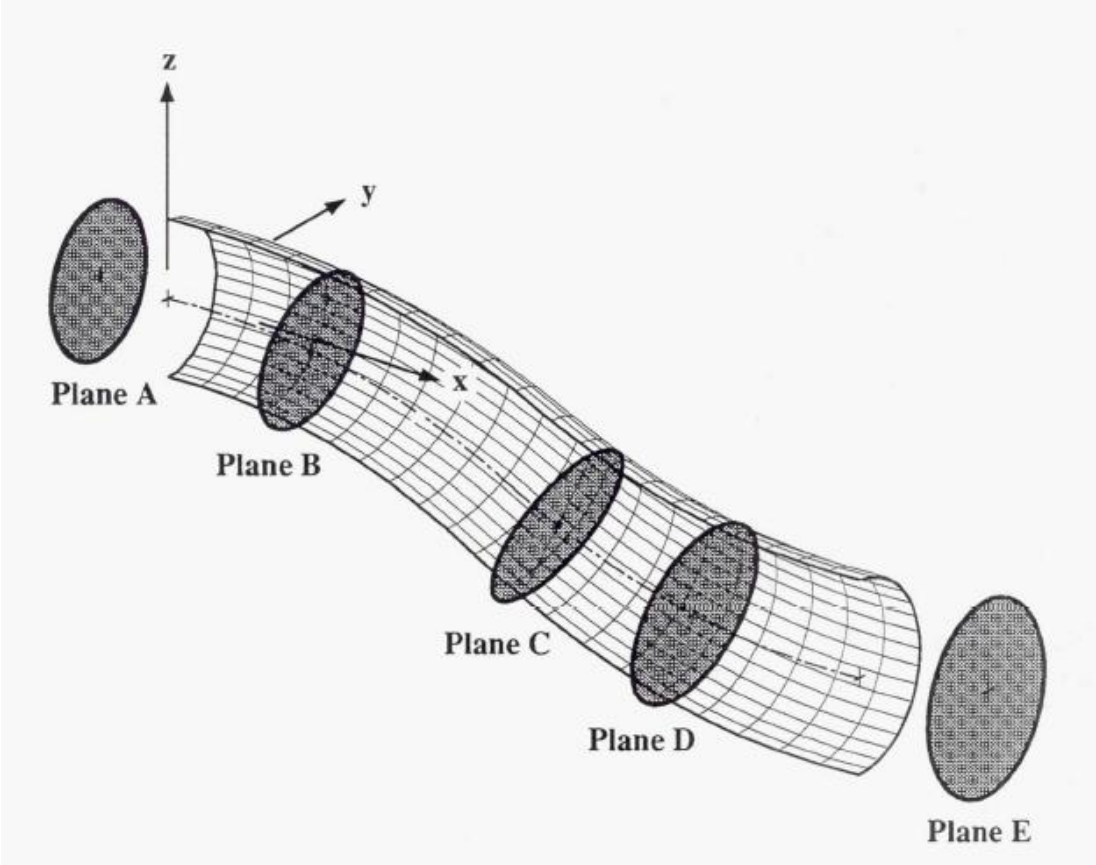

Figure 3.1 NASA Glenn S-Duct reference planes for comparison of experimental and computational results [1]

For the AIAA PAW S-duct, these planes will have the same non-dimensional coordinates due to scaling. However, the physical coordinates will differ, except the inlet coordinate $s/D_1=0$. This is important to know when comparing the results of two S-ducts.

3.2 Solution Convergence in Numerical Simulations

The first criterion used in all simulations was to achieve a steady mass flow rate at the reference inlet plane as prescribed by the NASA Glenn Research Center experiment [3]. Next, the solution residuals were monitored to assure the convergence of the solution. For the NASA Glenn Research Center case, the mass flow rate boundary condition applied at the computational domain outlet was determined by the reference inlet achieving a fully developed flow of Mach number M = 0.6. For the AIAA PAW case, the mass flow rate was also monitored at the AIP. Once the desired mass flow rate in the reference plane of each case was established, the simulations were continued until there was no apparent change in the total pressure or Mach number in the separated flow region and the residuals dropped by six-orders of magnitude.

3.3 Flow Properties Considered in Comparison of Experimental and Numerical Results

Based on the availability of experimental data, the comparisons between the experimental and numerical results were made for the variations in Mach number, static pressure coefficient, and total pressure coefficient in the flow field.

For compressible flow, Fluent automatically calculates the Mach number. For incompressible flow, on the other hand, one needs a User Defined Function (UDF) to calculate the Mach number which is given in Appendix A.

Static and total pressures are expressed using the non-dimensional pressure coefficients given by Equations 3.1-3.2. Local static pressure is denoted by p and the local total pressure is denoted by p_o, the reference values of static and total pressures are defined at the inlet centerline by p_{cl} and $p_{o,cl}$ respectively.

$$C_p = \frac{p - p_{cl}}{p_{o,cl} - p_{cl}} \tag{3.1}$$

$$C_{po} = \frac{p_o - p_{cl}}{p_{o,cl} - p_{cl}} \tag{3.2}$$

In order to plot the total pressure coefficient contours, a UDF was created which is given in Appendix B. This UDF takes into account the compressibility effects and calculates the speed of sound, Mach number, and total pressure using the standard compressible flow equations given by Equations 3.3-3.5. With these quantities calculated, the total pressure coefficient, C_{po}, is evaluated. Both UDFs in Appendix A and B are employed once the solution converges and is ready for analysis. Mach number and the total pressure calculated by the UDFs is compared with that calculated automatically by Fluent for compressible flow in order to ensure that proper numerical data is used when calculating the total pressure coefficient C_{po}.

$$\text{Speed of Sound } a = \sqrt{\gamma \frac{p}{\rho}} \tag{3.3}$$

$$Mach\ Number\ M = \frac{\sqrt{u^2 + v^2 + w^2}}{a} \tag{3.4}$$

$$Total\ Pressure\ p_o = p\left(1 + \frac{\gamma - 1}{2} M^2\right)^{\frac{\gamma}{\gamma - 1}} \tag{3.5}$$

Chapter 4

NASA Glenn Research Center S-Duct Analysis: Comparison of Experimental and Numerical Results

The results of the numerical simulation of both compressible and incompressible flow for the NASA Glenn Research Center S-Duct case are presented in this chapter. The effects of compressibility on pressure coefficient are evaluated in order to better understand the flow physics inside the S-Duct. The effects of four different turbulence models on solution accuracy are evaluated.

4.1 Experimental Results

Experimental results of static pressure coefficient from the NASA Glenn experiment are shown in Figure 4.1. Static pressure coefficient has been plotted along the surface of the duct at three angular locations - at the top (ϕ=10°), in the middle (ϕ=90°), and at the bottom (ϕ=170°). Figure 4.1 shows the variation in static pressure coefficient along the duct at these three angular locations. The first bend located between s/D1 = 0 and s/D1=2 of the duct shows an overall pressure rise along all the three angular sections. This rise is caused by the streamline curvature and diffusion [3]. The effect of separated flow is indicated by the nearly constant values of static pressure coefficient at the bottom and middle sections (ϕ=170° and ϕ = 90°) from s/D1=2.3 to s/D1=3.2 [3]. It is worth noting that a uniform static pressure region exists at s/D1=2.6; the static

pressure coefficients are the same at all angular locations. Once the flow reattaches, around s/D1= 3.2, the pressures begin to rise again.

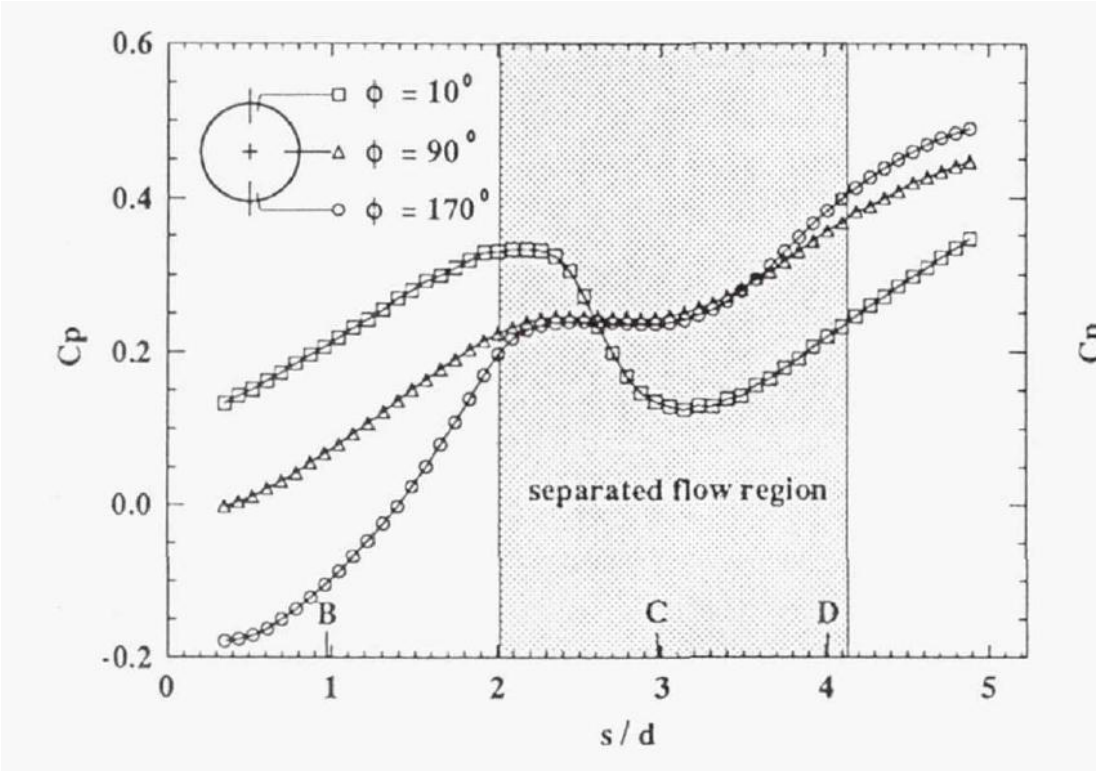

Figure 4.1 Experimental static pressure coefficients along the S-duct at different angular locations in NASA Glenn experiment [1]

In the experiment, the flow features inside the S-Duct were captured in the form of streak-lines using the fluorescent oil. The streak-line patterns lead to three conclusions. First, the flow is symmetric as can be seen from Figure 4.2 [3, 5]. Second, a large region of flow separation exists at the bottom part of duct after the first bend [3, 5]. Figures 4.3 and 4.4 show the separated flow through the surface oil flow streak-lines patterns on the duct wall and in the symmetry plane. Third, the transverse secondary flows exist [3, 5]. These observations are characteristic traits of the flow through diffusing S-ducts.

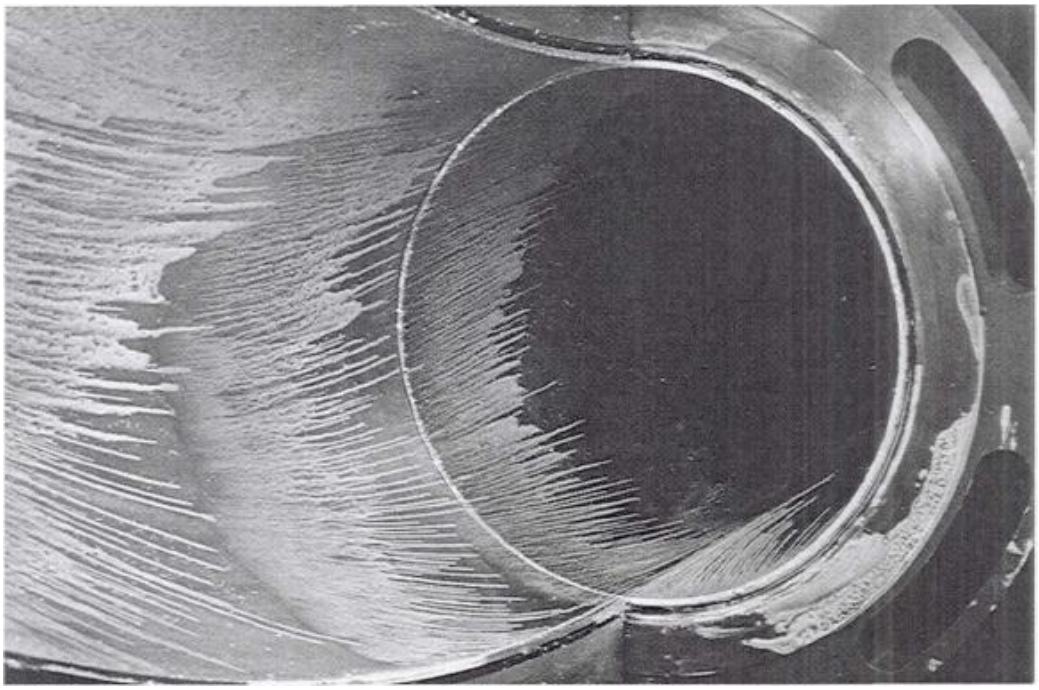

Figure 4.2 Surface oil flow streak-lines at duct exit showing the flow symmetry [5].

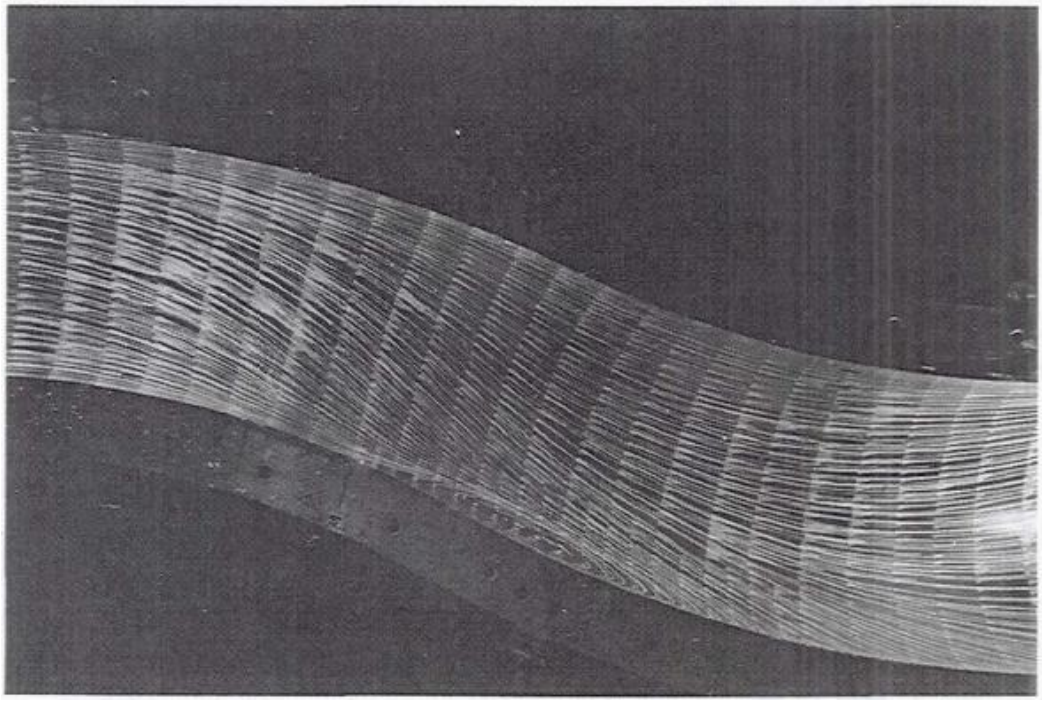

Figure 4.3 Surface oil flow streak-lines on a middle cross-sectional plane of the S-Duct showing flow separation at the bottom surface [5].

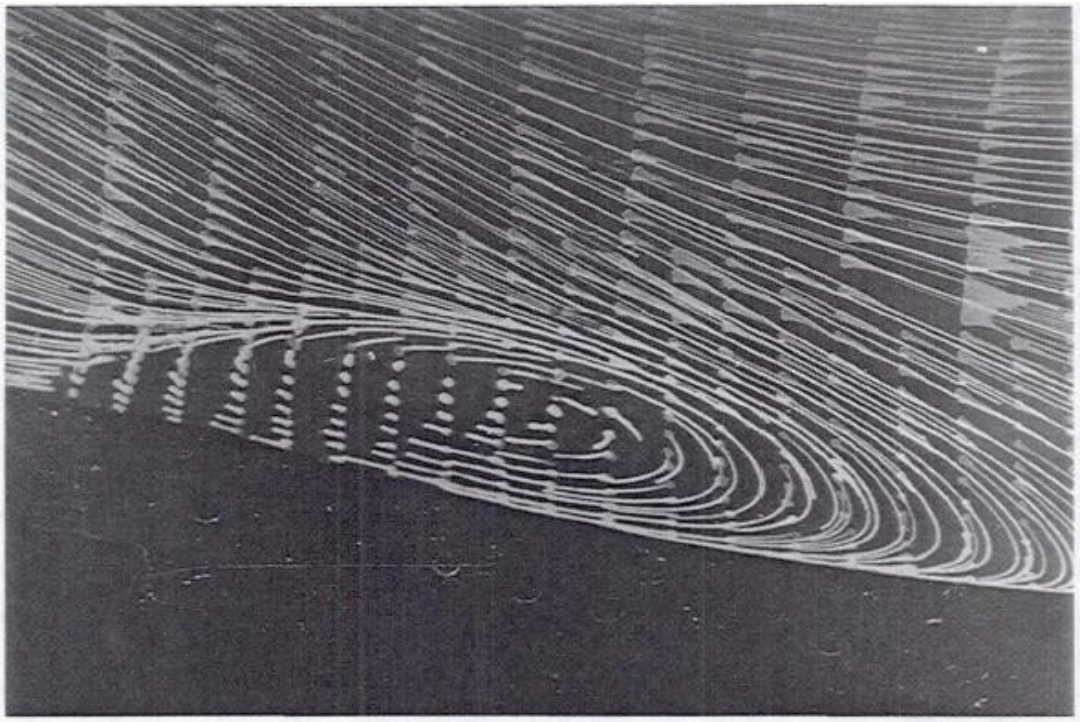

Figure 4.4 Close up view of surface oil flow streak-lines on the bottom surface of the duct showing the recirculating flow in the separated region [5].

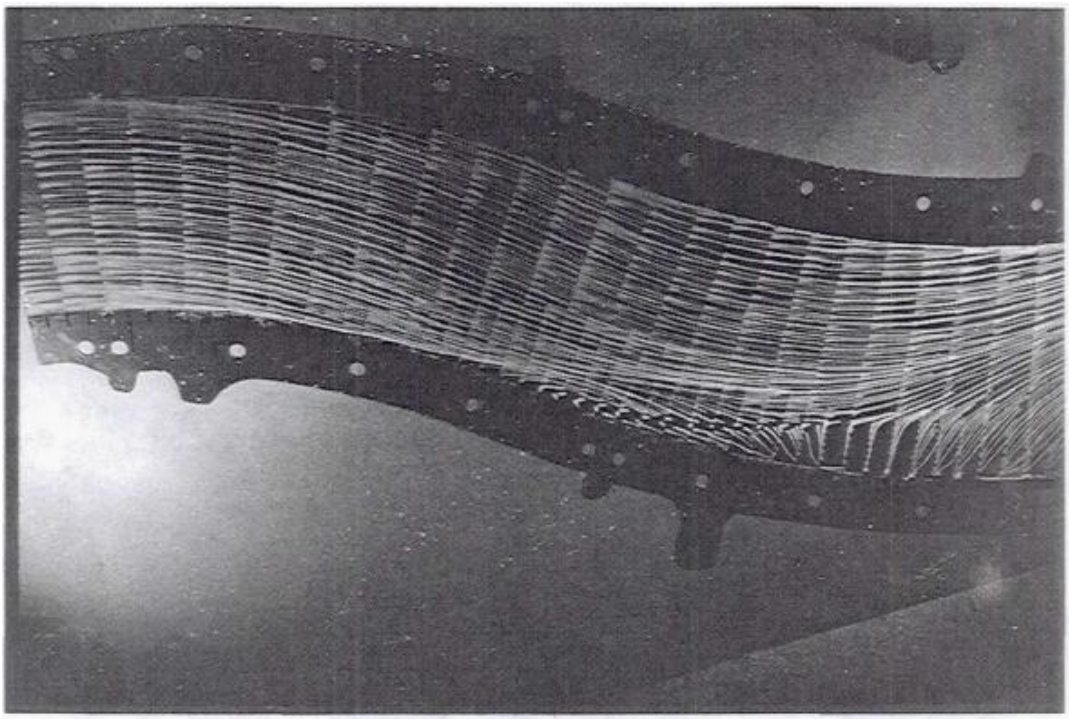

Figure 4.5 Surface oil flow streak-lines in the symmetry plane [5].

4.2 Boundary Layer Characteristics

The boundary layer formation characteristics need to be matched in order to fully compare the experimental results with the computational simulations. Figure 4.6 compares the computed boundary layer velocity profile with the experimental velocity profile at the reference inlet plane of the duct using the non-dimensional variables for the axial velocity component u^+ and the distance from wall y^+. The computed and experimental boundary layer velocity profiles are in acceptable agreement thus validating our modeling assumptions. The equations for u^+ and y^+ are dependent upon a quantity, u^*, which relates the wall shear stress τ_w and density ϱ as given in Equation 4.1. The wall shear stress τ_w is a function of kinematic viscosity υ, the wall distance y and the axial velocity component u. These quantities are defined in Equations 4.1, 4.2, and 4.3 [1].

$$u^* = \sqrt{\frac{\tau_w}{\rho}} \tag{4.1}$$

$$u^+ = \frac{u}{u^*} \tag{4.2}$$

$$y^+ = \frac{u^* y}{\nu} \tag{4.3}$$

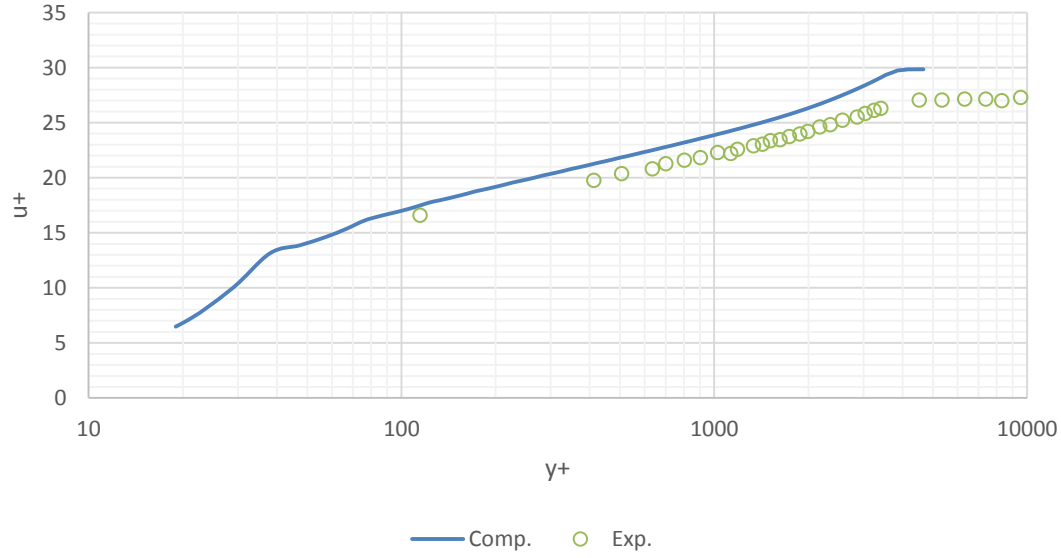

Figure 4.6 Comparison of computed and experimental non-dimensional boundary layer velocity profile, experimental data is from NASA Glenn test.

4.3 Numerical Results (Incompressible Flow)

In order to assess the effects of compressibility; both compressible and incompressible solutions are computed and compared. Effects of four different turbulence models on solution accuracy are also evaluated. Incompressible flow assumes that density is constant throughout the computational domain. This assumption may be valid at lower flow velocities; however the NASA Glenn experiment has flow condition of Mach number M = 0.6 at the reference inlet plane which is in the compressible regime. Therefore the compressibility should be considered; but we compute both the incompressible and compressible flow to determine the effects of compressibility.

4.3.1 Computations with Spalart-Allmaras Turbulence Model

The first turbulence model employed in the simulation was the one-equation Spalart-Allmaras (SA) model. Figure 4.6 shows the static pressure coefficients along the duct for the three angular sections. From Figure 4.6, it can be noticed that the computed static pressure coefficient along the duct at top angular section (ϕ=10°) compares well with the experimental static pressure coefficient, although it is slightly higher. The pressure coefficient begins to diverge from the experimental data at s/D_1=2.5m and again becomes closer to it at s/D_1=4.5 m. Similarly at the middle angular position (ϕ=90°), static pressure coefficient initially follows the experimental data quite well, but begins to diverge at s/D_1=2 and again becomes closer to it at s/D_1=4.5. At the bottom angular position (ϕ=170°), static pressure coefficient does not agree very well with the experimental data. Figure 4.6 shows that the computed pressure coefficient lags the experimental data and becomes closer to it at the end of the S-Duct around s/D_1=5. The Spalart-Allmaras turbulence model overall predicts the static pressure coefficient

reasonably well but struggles to compute it accurately in the area where complex flow phenomena such as separation occur near the bottom portion of the duct.

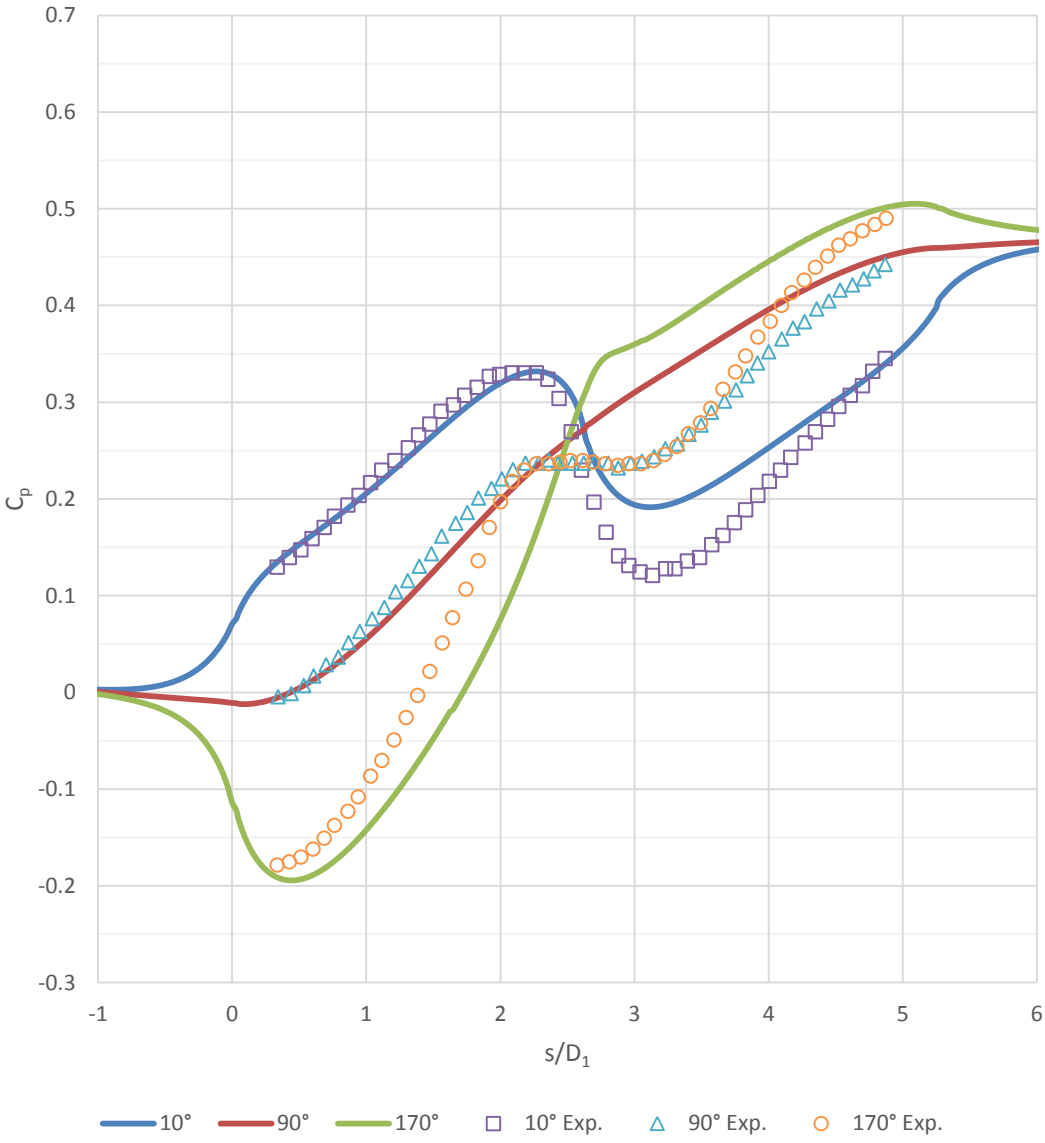

Figure 4.7 Comparison of experimental and computed (with SA turbulence model) static pressure coefficients in incompressible flow along the duct at three angular locations: ϕ=10°, ϕ=90° and ϕ=170°

4.3.2 Computations with k - ε Turbulence Model

Next set of computations were performed using the k-ε turbulence model. It is clear from Figure 4.7 that it suffers from the same inaccuracies in predictions as the SA model in the same areas of the duct. The computed solution in the top angular section, ϕ=10°, appears to be slightly closer to the experimental static pressure coefficient from s/D_1=0 to s/D_1=2, compared to the SA model predictions in Figure 4.6. However, from s/D_1=2 to s/D_1=5, it is less accurate than the SA model for the top angular section ϕ=10°. The computed results in the middle angular section, ϕ=90°, also seem to be more accurate compared to SA results from the s/D1=0 to s/D1=2. For the bottom angular section, ϕ=170°, although the pressure coefficient shapes are slightly different, both the k-ε and SA give inaccurate results for the entire length of s/D_1.

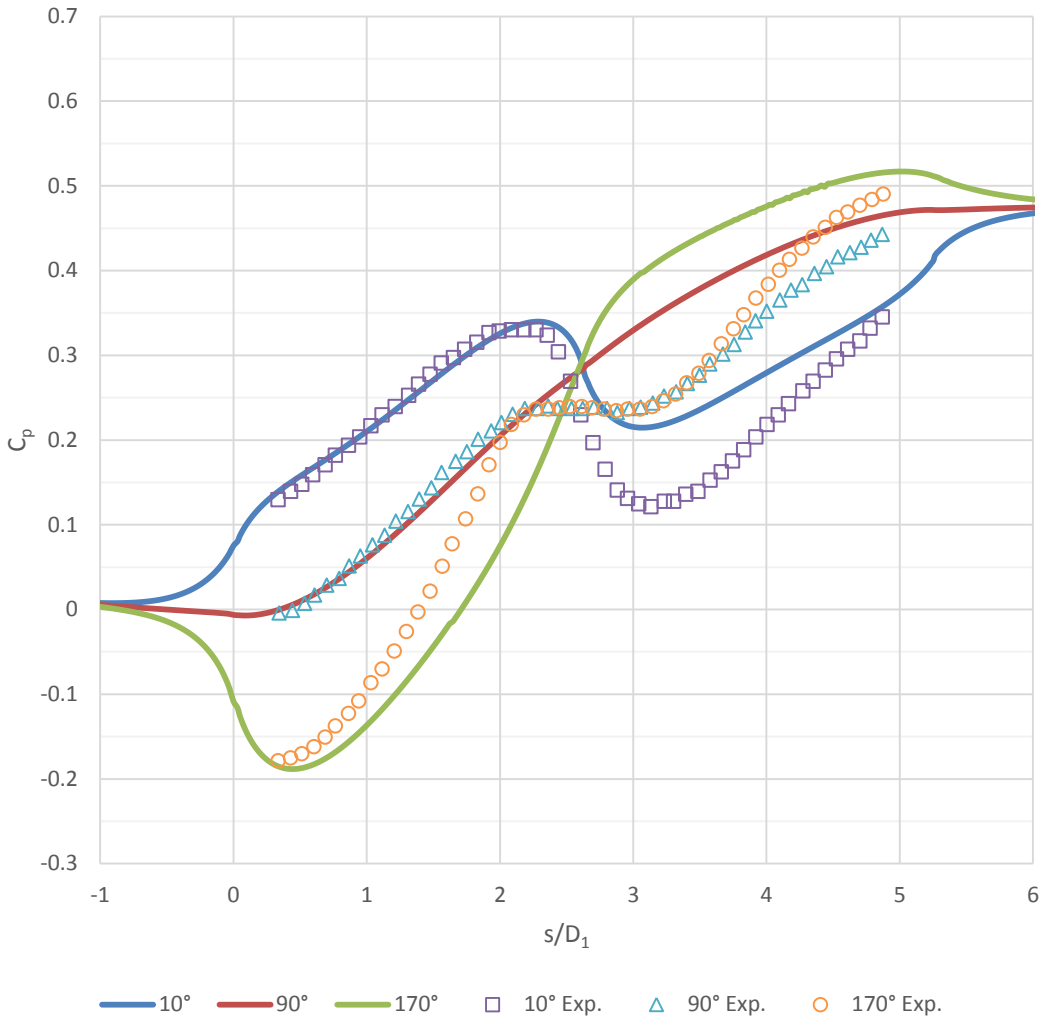

Figure 4.8 Comparison of experimental and computed (with k - ε turbulence model) static pressure coefficients in incompressible flow along the duct at three angular locations: ϕ=10˚, ϕ=90˚ and ϕ=170˚

4.3.3 Computations with k-ω SST Turbulence Model

The k-ω SST turbulence model, as shown in Figure 4.8, predicts the static pressure coefficients very similar to the SA model. Its predictions however are much better than those of the k-ε model in all angular sections. The predictions of k- ω SST model are

almost identical to that of the SA model in the top (ϕ=10°) and middle (ϕ=90°) angular sections of the duct, but it becomes more accurate in the bottom angular section (ϕ=170°) compared to SA model. Overall the predictions of k-ω SST model are closer to the experimental results compared to those obtained with SA and k – ε model.

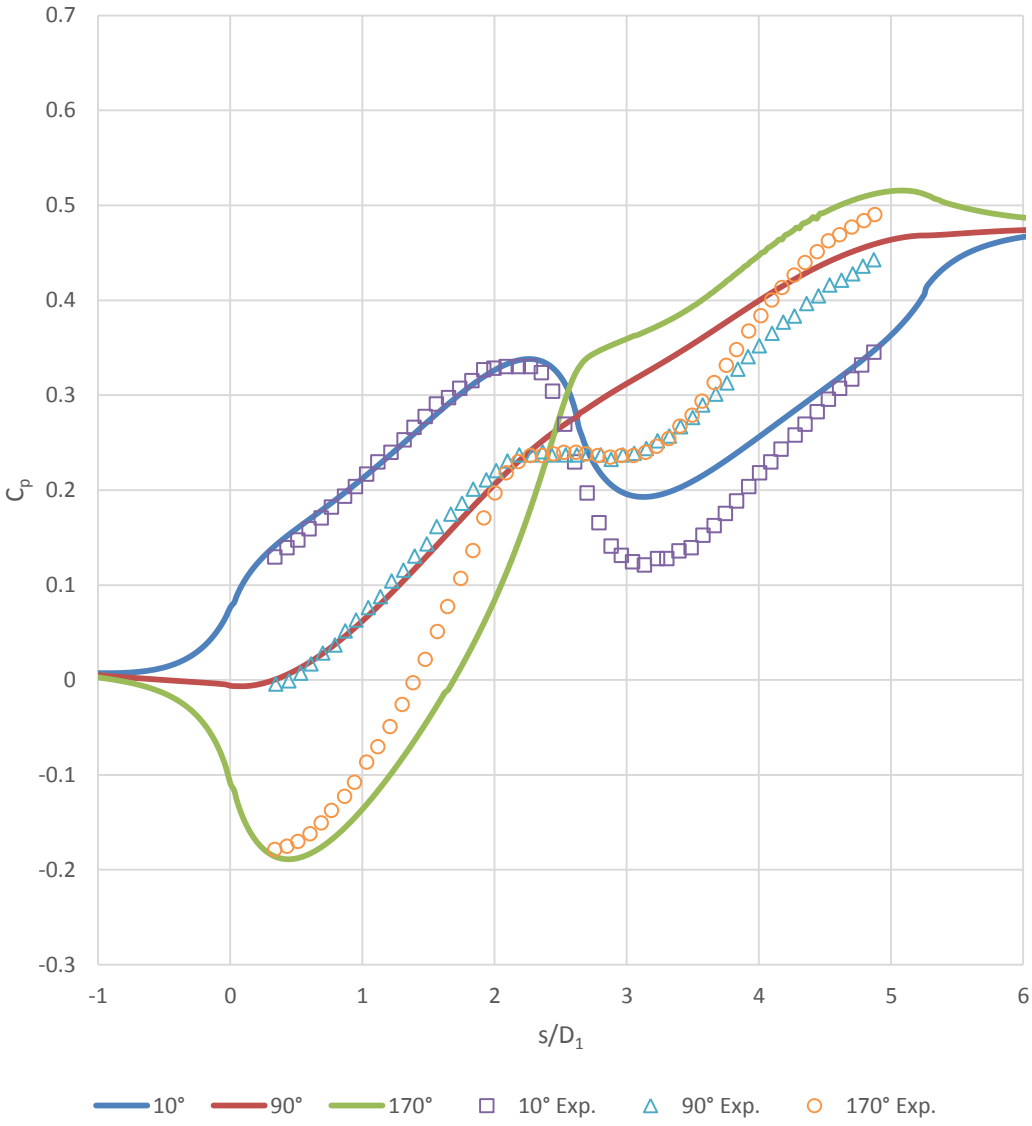

Figure 4.9 Comparison of experimental and computed (with k-ω SST turbulence model) static pressure coefficients in incompressible flow along the duct at three angular locations: ϕ=10°, ϕ=90° and ϕ=170°

4.3.4 Computations with Transition SST Turbulence Model

The Transition SST turbulence model has four transport equations. It does the best job in predicting the static pressure coefficient along the duct for each angular location. From Figure 4.9 it is evident that all static pressure coefficients are closer to the experimental values. The computed static pressures are still higher than the experimental values throughout the duct, but start to converge towards the experimental values at s/D_1 equal to or greater than 5.

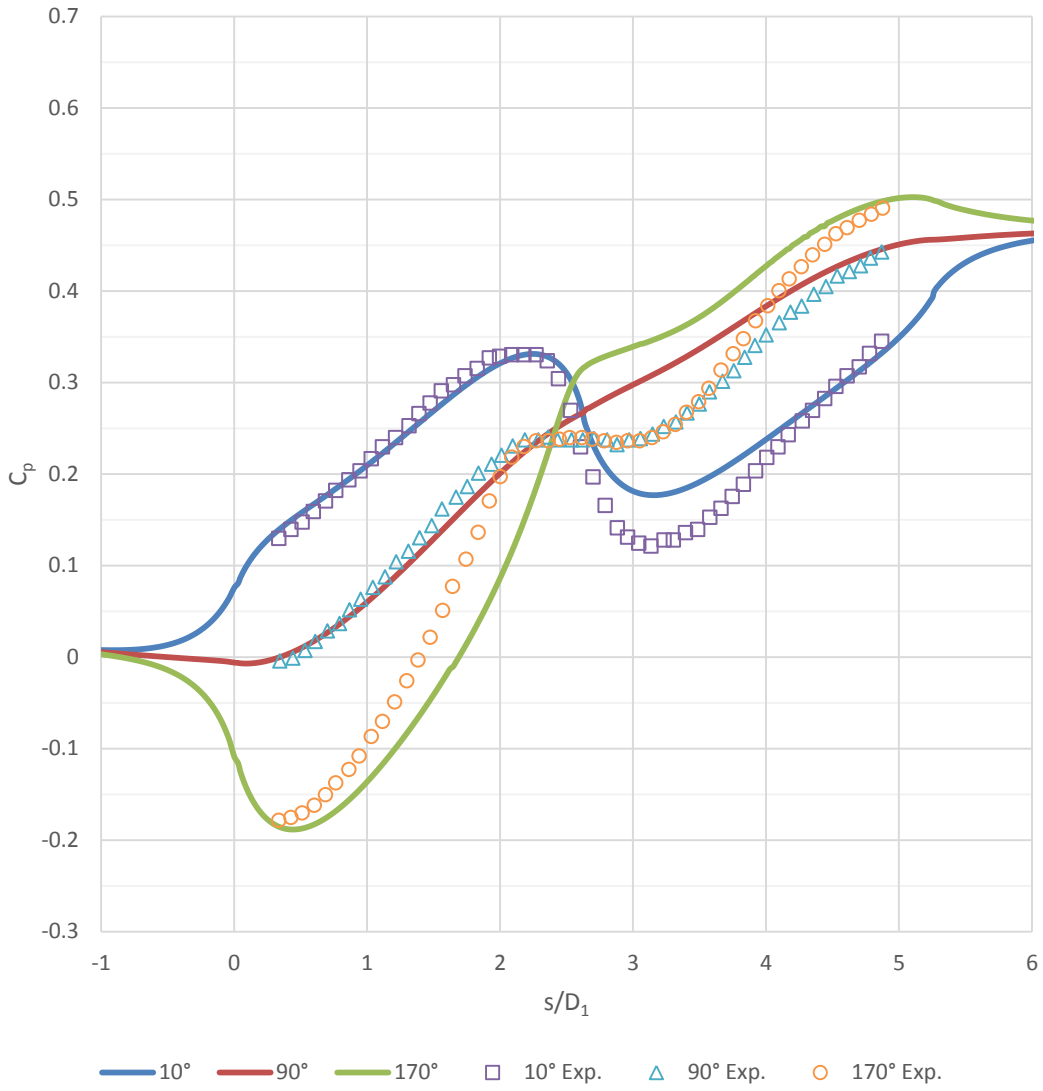

Figure 4.10 Comparison of experimental and computed (with Transition SST turbulence model) static pressure coefficients in incompressible flow along the duct at three angular locations: ϕ=10°, ϕ=90° and ϕ=170°

4.3.5 Summary of Computed Incompressible Flow Results

By comparing the static pressure coefficients in Figures 4.6-4.9 using four different turbulence models, one can notice a trend. All the models predict the static pressure

coefficient along the duct quite well in top (ϕ=10°) and middle (ϕ=90°) angular locations; however they all lack accuracy at the bottom angular (ϕ=170°) location when compared to the experimental data. The bottom part of the duct experiences flow separation due to curvature, therefore it is a difficult area to resolve for the experiment and the simulation. It should be noted that all the models exhibit almost a similar value for the static pressure coefficient at s/D1=2.6, much like the experimental result. In summary, all four turbulence models used in steady incompressible flow calculation of the flow field inside the S-duct produce inaccurate results near the bottom part of the duct. Among all four models, the Transition SST model predicted the most accurate static pressure coefficients when compared to the experimental values.

4.4 Numerical Results (Compressible Flow)

In compressible flow simulations, density varies throughout the computational domain and the air is considered to obey the ideal gas law. Because the Mach number at the reference inlet is M = 0.6, it is unlikely to become higher in other parts of the duct, since it is diffusing. Therefore the entire flow field remains subsonic without the appearance of any shocks. The Mach number at the reference inlet is important since it is needed to correctly match the experimental flow conditions.

4.4.1 Computations with Spalart-Allmaras Turbulence Model

Again as in the case of incompressible flow, the first turbulence model considered in calculation of steady compressible flow in the S-duct is the SA one-equation model. Figure 4.10 provides the computed static pressure coefficients along the duct at three angular locations (ϕ=10°, ϕ=90° and ϕ=170°). Comparing with the incompressible flow results in Figure 4.6, it is clear that the compressible flow results are in better agreement with the experimental data. From s/D_1=0 to s/D_1=2, at all angular locations (ϕ=10°,

ϕ=90° and ϕ=170°), the static pressure coefficients are almost identical to experimental values. From s/D_1=2 to 5 the computed pressures are higher than the experimental values but have a shape similar to that in the experiment. The bottom section of the duct (ϕ=170°) has a small region located between s/D_1=2.6 to 2.8, which is similar to the experiment where the boundary layer separation occurs.

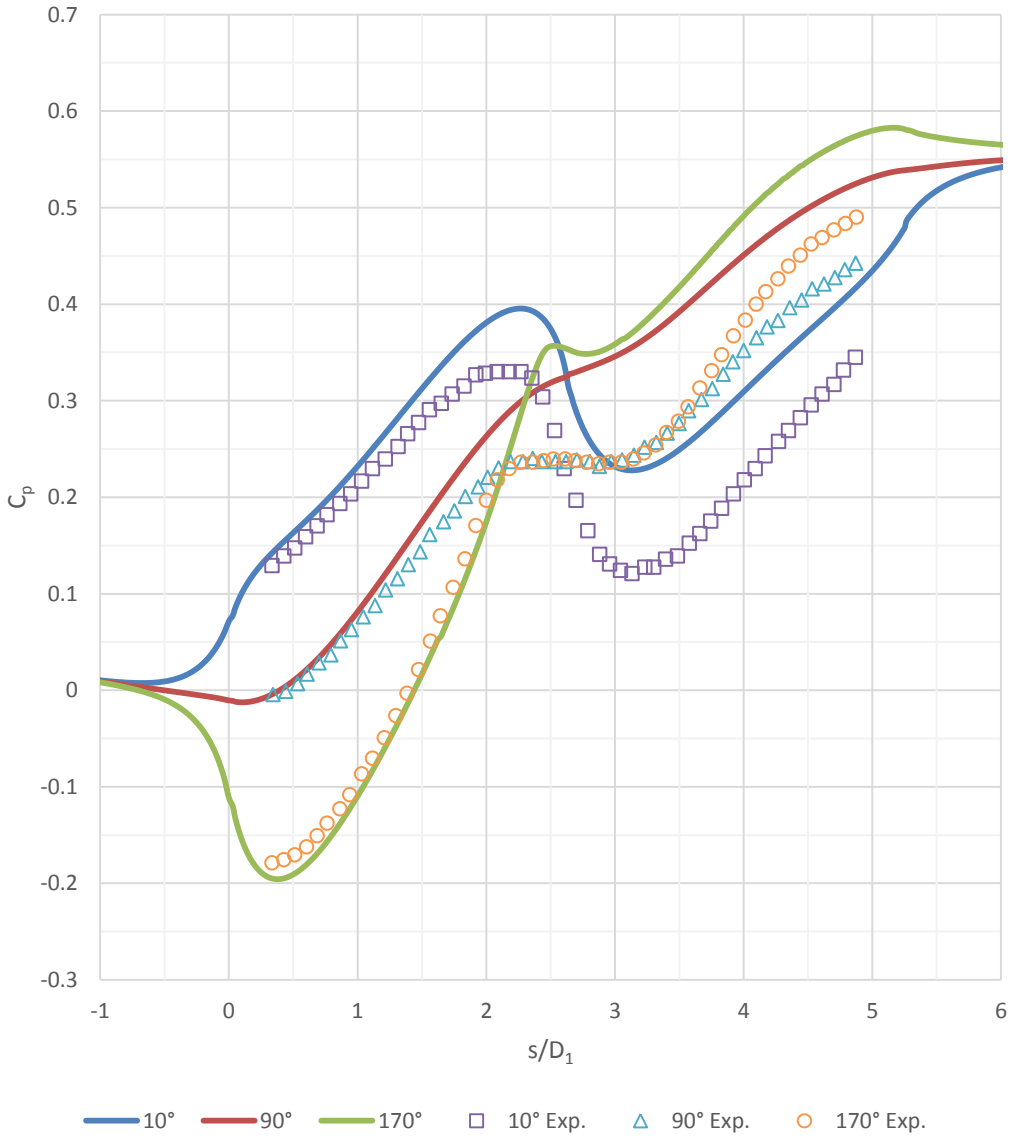

Figure 4.11 Comparison of experimental and computed (with SA turbulence model) static pressure coefficients in compressible flow along the duct at three angular locations: ϕ=10°, ϕ=90° and ϕ=170°

4.4.2 Computations with k-ε Turbulence Model

Just like in case of incompressible flow, the compressible flow calculations using the k-ε turbulence model do not compare well with the experimental data compared to other turbulence models. Figure 4.11 shows that after $s/D_1=1.5$ the model fails to accurately predict the static pressure coefficient. The pressure coefficient at the top angular location ($\phi=10^\circ$) of the duct is well predicted; however it is much higher than that predicted from other turbulence models. The predictions for the middle ($\phi=90^\circ$) and bottom ($\phi=90^\circ$) angular locations are not accurate at all in values or shape of the pressure curves.

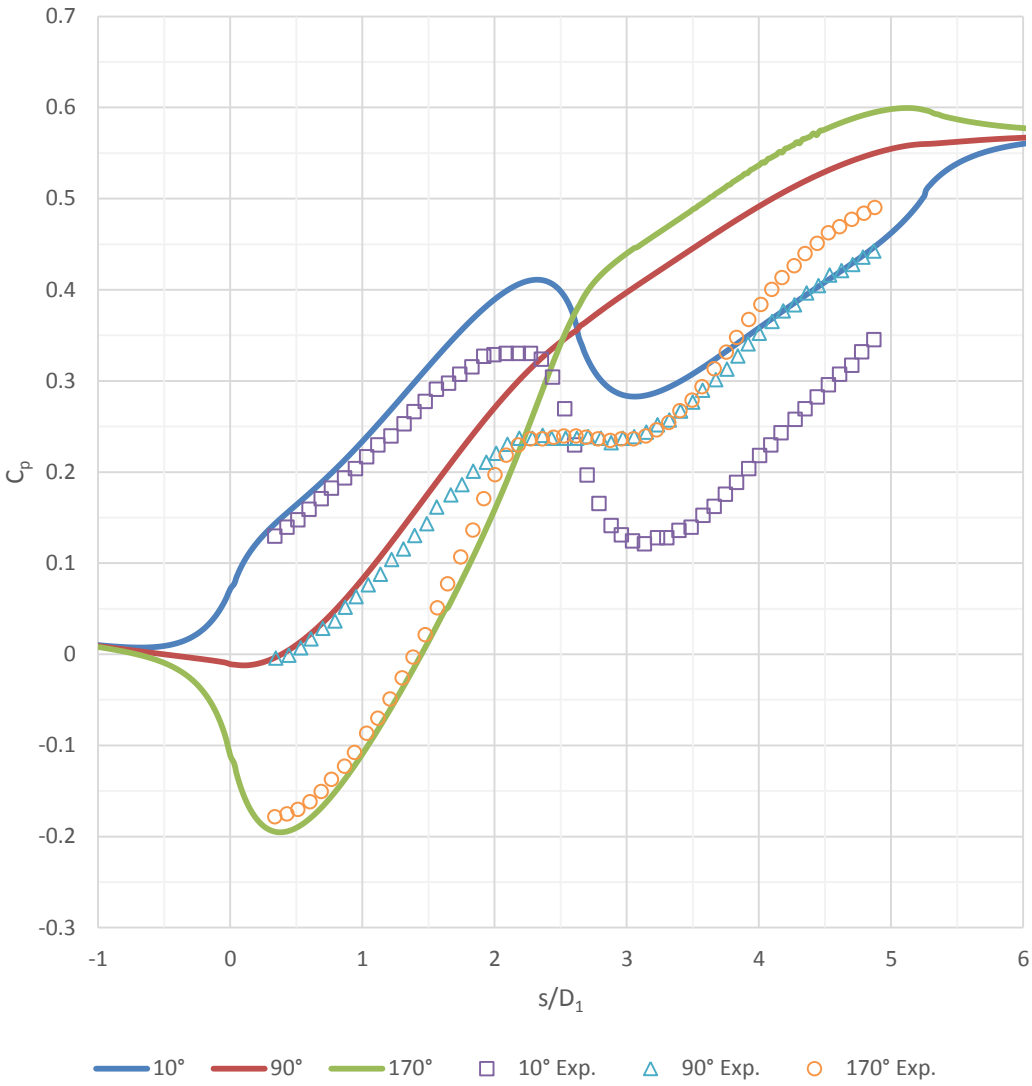

Figure 4.12 Comparison of experimental and computed (with k-ε turbulence model) static pressure coefficients in compressible flow along the duct at three angular locations: ϕ=10°, ϕ=90° and ϕ=170°

4.4.3 Computations with k-ω SST Turbulence Model

The k-ω SST model is much more accurate in predicting the static pressure coefficients compared to SA and k-ε models, although the predicted pressures are higher than the

experimental values, as shown in Figure 4.12. The pressure coefficient at top angular location (ϕ=10˚) is very similar to that in the experiment. The shapes of the computed pressure coefficients at middle (ϕ=90˚) and bottom (ϕ=170˚) angular locations are also very similar. At both of these angular locations, there is a constant static pressure coefficient region from s/D_1=2.5 to s/D_1=3.2 indicating flow separation. This correlates well with the experimental results, however in computations the region of separation occurs slightly later in the duct.

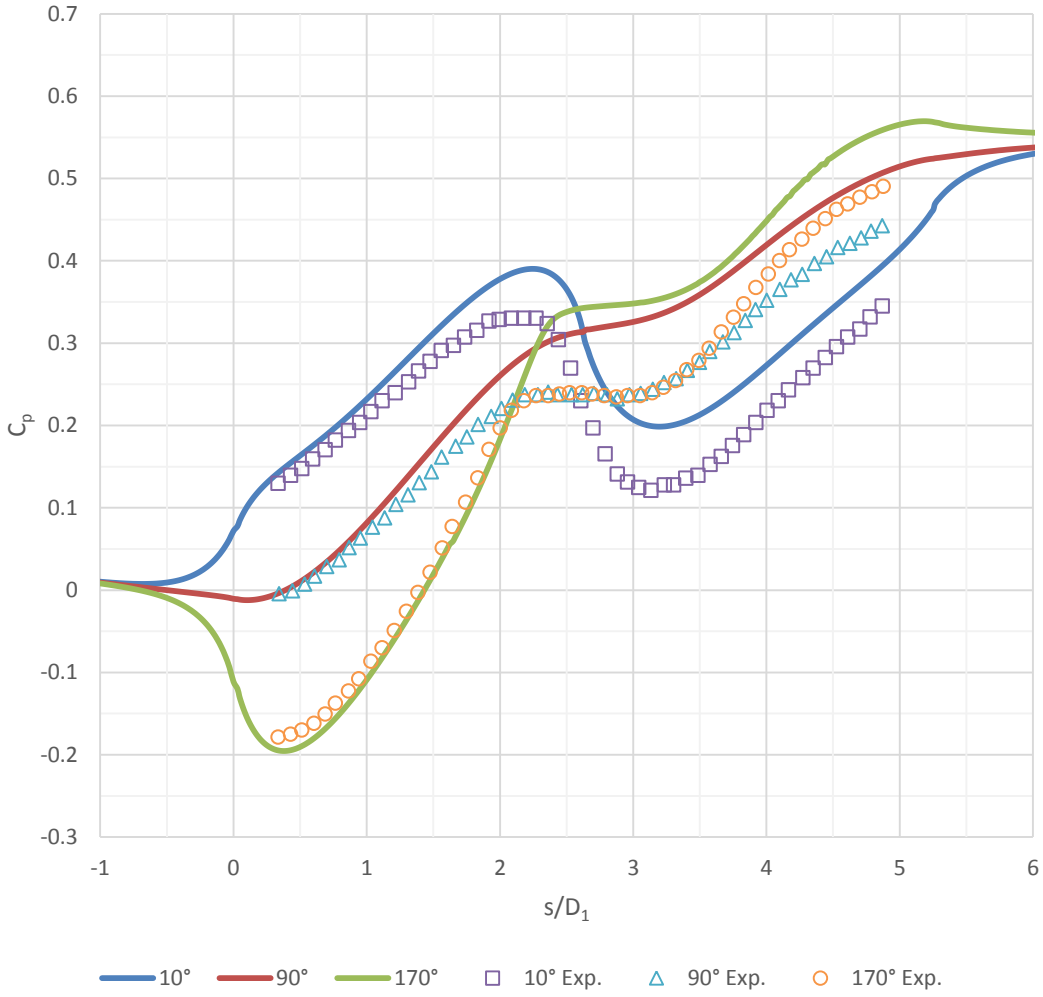

Figure 4.13 Comparison of experimental and computed (with k-ω SST turbulence model) static pressure coefficients in compressible flow along the duct at three angular locations: ϕ=10˚, ϕ=90˚ and ϕ=170˚

4.4.4 Computations with Transition SST Turbulence Model

Just like in the incompressible flow case, the Transition SST turbulence model does a very good job in predicting the static pressure coefficient in steady compressible flow as shown in Figure 4.13. Again like in case of incompressible flow, its results are very similar to the k-ω SST model. The values for the static pressure coefficient in the top angular location (ϕ=10°) of the duct are higher than the k-ω SST model results beyond s/D_1=2. This is the case for the middle (ϕ=90°) and bottom (ϕ=170°) angular locations as well. The constant static pressure region for the middle and top angular locations appears to be relatively smaller, spanning from s/D_1 =2.5 to s/D_1=3.0.

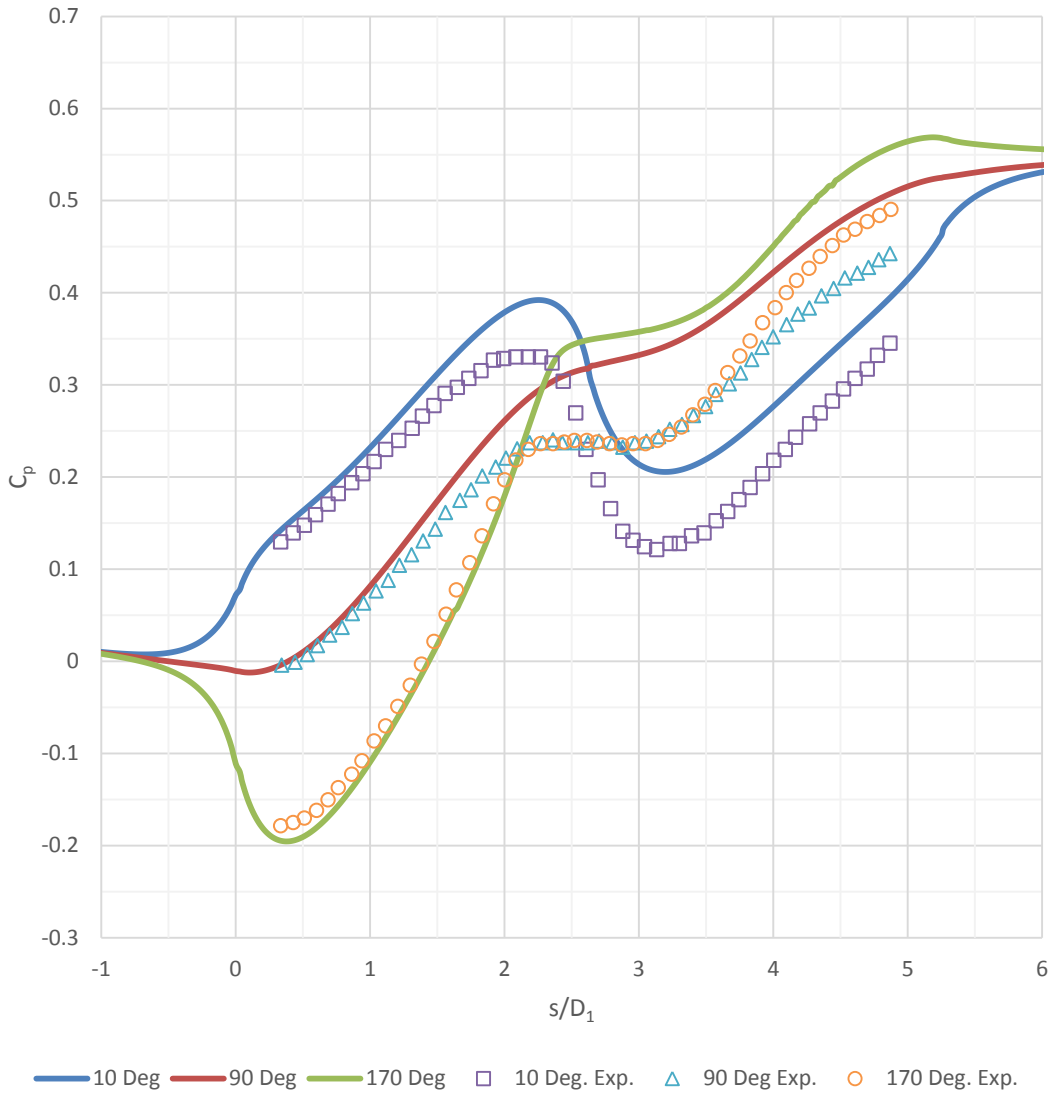

Figure 4.14 Comparison of experimental and computed (with Transition SST model) static pressure coefficients in compressible flow along the duct at three angular locations: ϕ=10°, ϕ=90° and ϕ=170°

4.4.5 Summary of Compressible Flow Results

By examining the results of calculations using four different turbulence models in Figures 4.10-4.13, it is clear that the static pressure coefficients are better predicted by

considering the flow to be compressible (in contrast to considering it to be incompressible). It is important to note that the resolution of the flow field in the bottom angular location (ϕ=170°) is much better in compressible flow compared to that in incompressible flow, although the static pressure coefficients are still slightly higher than the experimental values. The k-ω SST performs the best out of the four turbulence models.

4.5 Additional Results using the k-ω SST Turbulence Model

Based on the results obtained in sections 4.2 and 4.3, we have selected the k-ω SST turbulence model as the model of choice for calculating the S-duct flow fields. The model employs only two transport equations in contrast to Transition SST model which employs four transport equations and gives results very close to those obtained by the k-ω SST model. This model predicted static pressure coefficients very close to those obtained by the most accurate turbulence model - the Transition SST model. In order to better understand other features of the flow field in the S-duct, contours of Mach number and total pressure coefficient are created in the reference inlet and AIP planes and the plane of symmetry of the entire duct.

The plane of symmetry for the entire duct provides a great deal of information about the flow field as well as the influence of various turbulence models in predicting the flow characteristics. Figure 4.14 shows the experimental streamlines along the plane of symmetry. These streamlines were obtained experimentally by introducing a thin plate bisecting the experimental S-duct. Because the thin plate introduces shear stress and small blockage, the comparison with the computations is qualitative [6]. Figure 4.15 shows the computational streamlines in the plane of symmetry. From inspection, the streamlines from the computations look very similar to those in the experiment including those in the separated flow region. The computational streamlines however

show the separation point slightly downstream of that predicted in the experiment. The computation model fails to predict the height of the separation bubble which is above the duct centerline in the experiment. Figure 4.16 shows a close up view of the separation region with inverted color contours created for the ease of viewing.

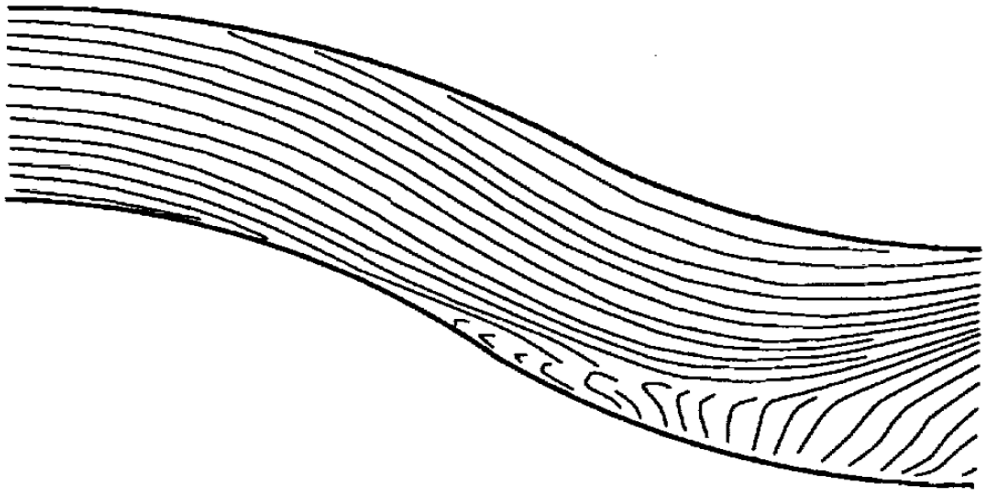

Figure 4.15 Experimental streamlines along the NASA Glenn S-duct [3]

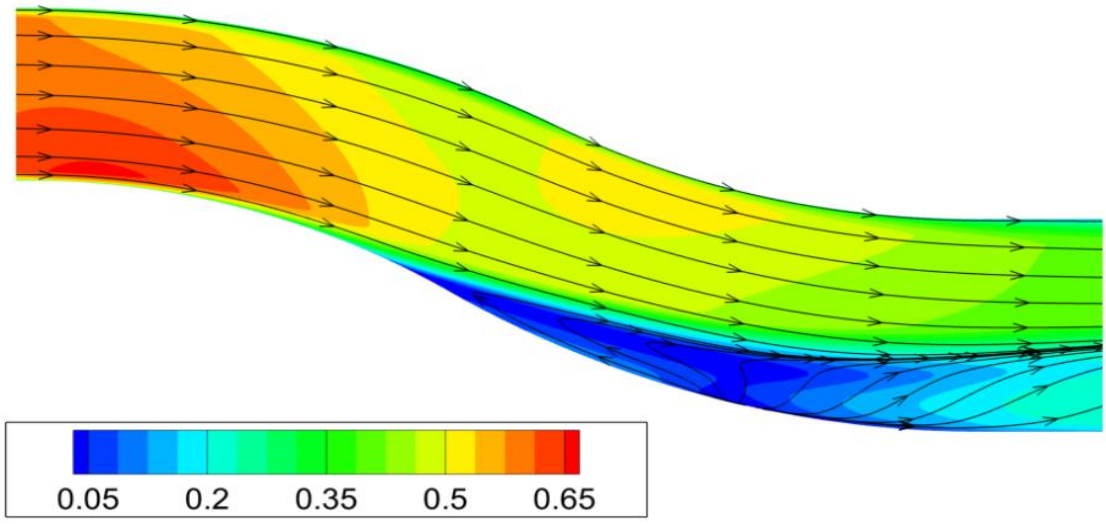

Figure 4.16 Computed streamlines along the NASA Glenn S-duct using the compressible flow assumption with k-ω SST turbulence model; color contours are of Mach number in the duct.

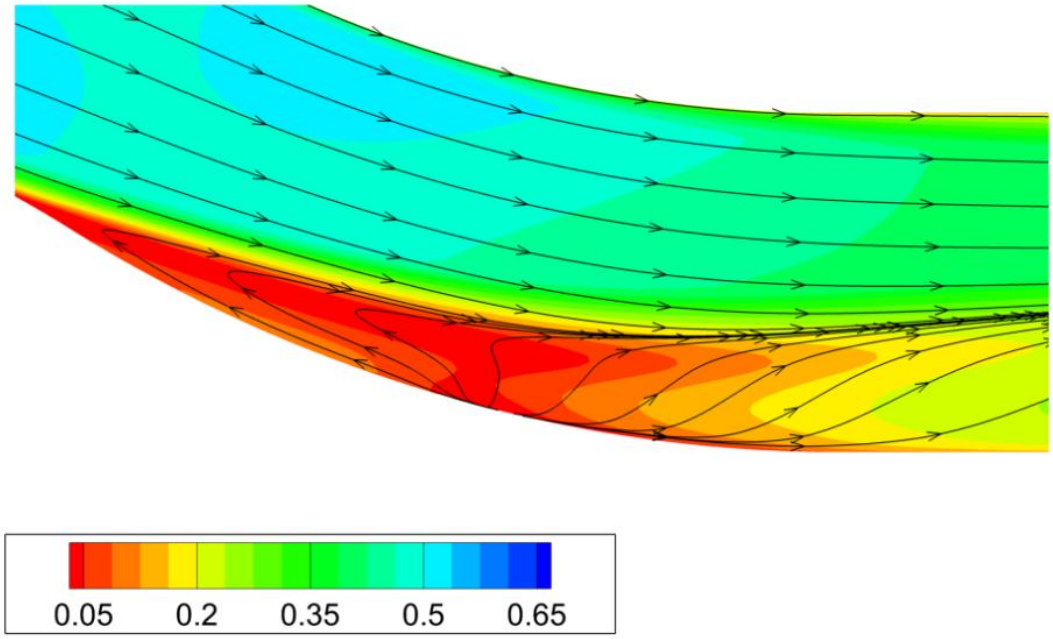

Figure 4.17 Zoomed-in-view of the computed streamlines along the bottom part of the NASA Glenn S-duct using the compressible flow assumption with k-ω SST turbulence model; color contours are of Mach number in the duct.

In order to better understand the flow field near the separation point and in the region of separation bubble, velocity vectors were plotted in the plane of symmetry and at angular location of ϕ=180º, these are shown in Figure 4.17. The computed separation point is at x = 0.415 m which corresponds to s/D1=2.097.

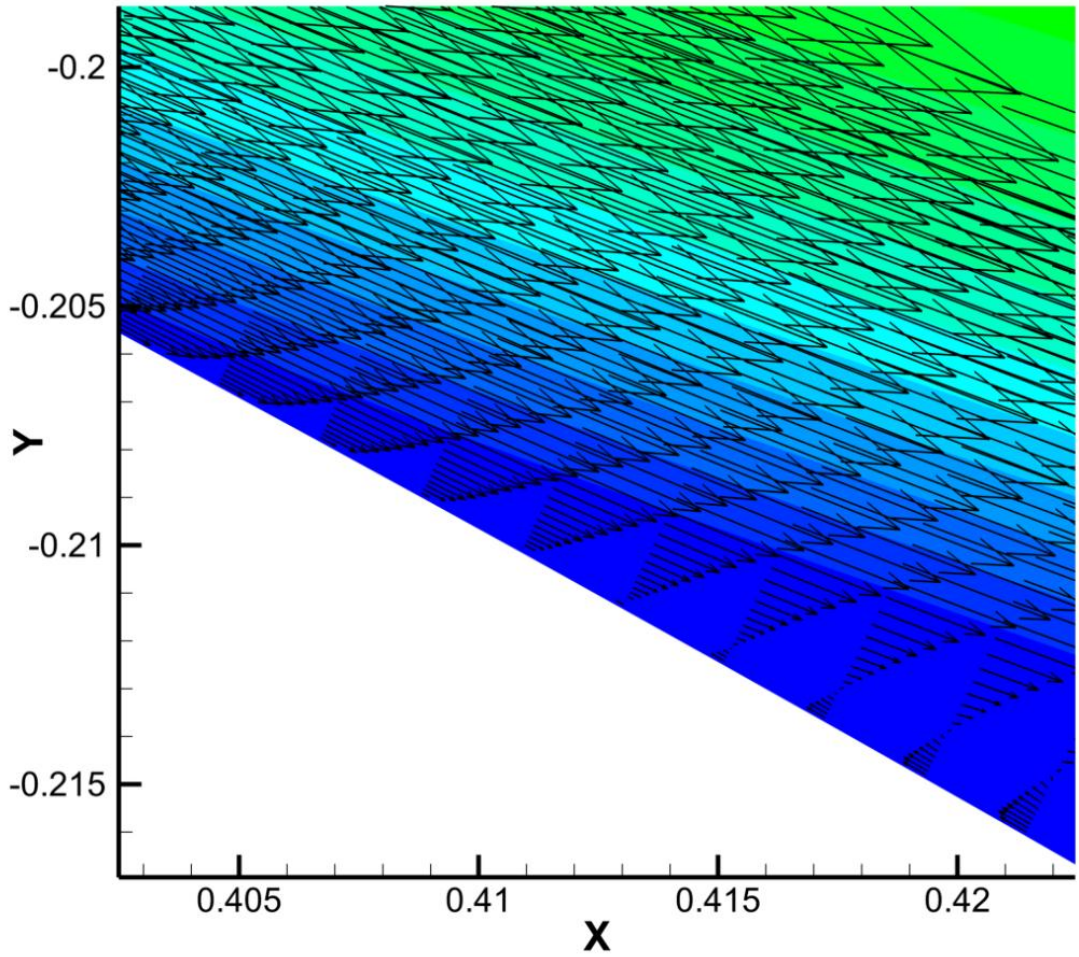

Figure 4.18 Computed velocity vectors in the plane of symmetry of the S-duct showing boundary layer separation at the bottom wall (indicated by arrows in the direction opposite to the main flow direction).

The flow in the reference inlet plane (at s/D_1=-0.5) is important to analyze in order to ensure that it corresponds to fully developed pipe flow. Figure 4.18 shows the Mach number contours in the reference inlet plane affirming that the flow is fully developed. The computed Mach contours in Figure 4.18 also verify that the flow conditions at the inlet match the experimental condition of maximum Mach number of M = 0.6. The uniform circular contours indicate that the flow is fully developed, free of vortices and the transverse velocity components.

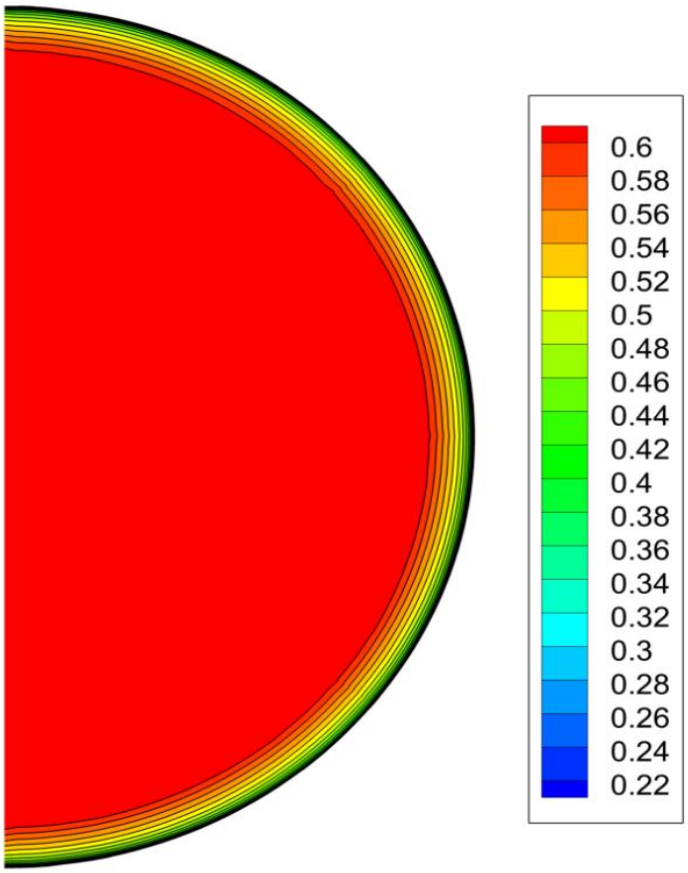

Figure 4.19 Computed Mach number contours at the reference inlet of NASA Glenn S-duct showing fully developed flow

The flow behavior at the aerodynamic interface plane (AIP) is very important since this is the plane where the duct interfaces with the turbine face. Uniform flow and adequate pressure recovery is desired in this plane. The comparison of the experimental and computed Mach number contours in this plane is shown in Figure 4.19. This Figure shows that the computed contours are very similar to those in the experiment. The shape of the contours are similar, however there are some quantitative differences. This can be attributed to the late separation predicted by CFD.

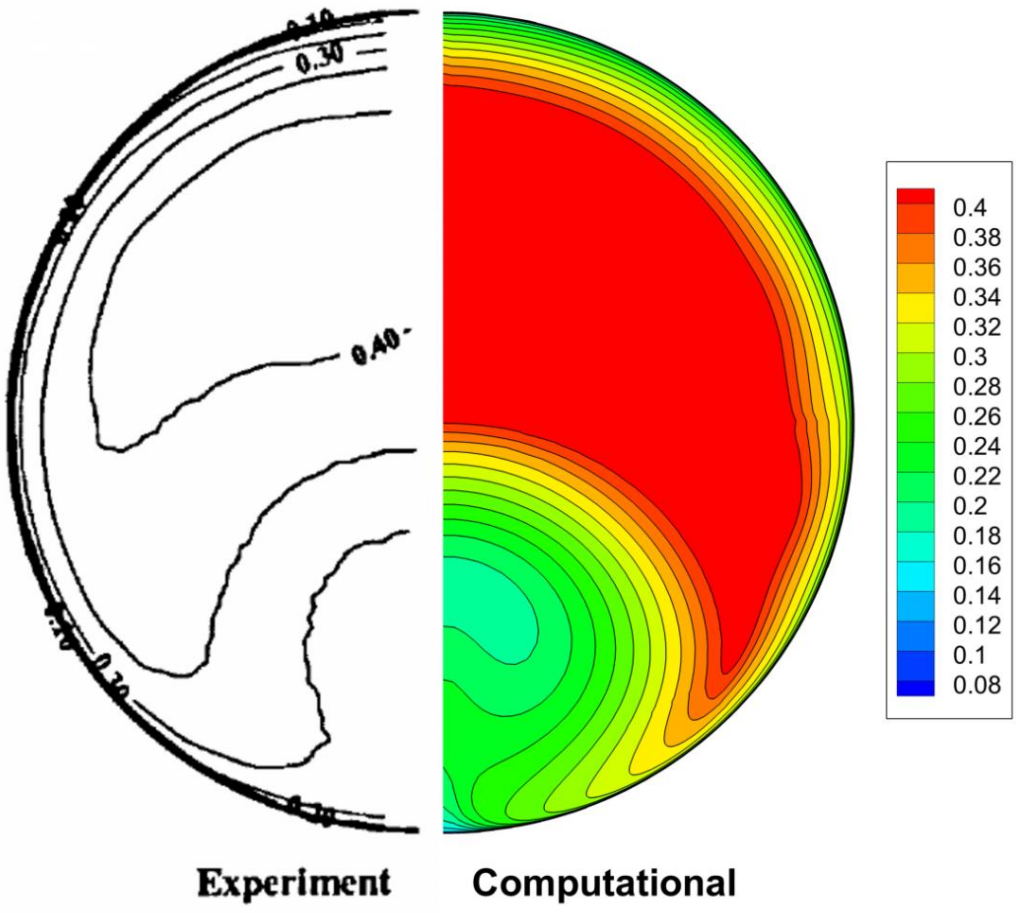

Figure 4.20 Experimental and computed Mach number contours in AIP

Total pressure contours in AIP are plotted in Figure 4.20. This figure shows that the pressure is not uniform across the AIP. The computed total pressure contours, much like the computed Mach contours in Figure 4.19, have lower value than the experimental value at same location in the duct. Again this lower value can be attributed to late prediction of separation in the CFD model.

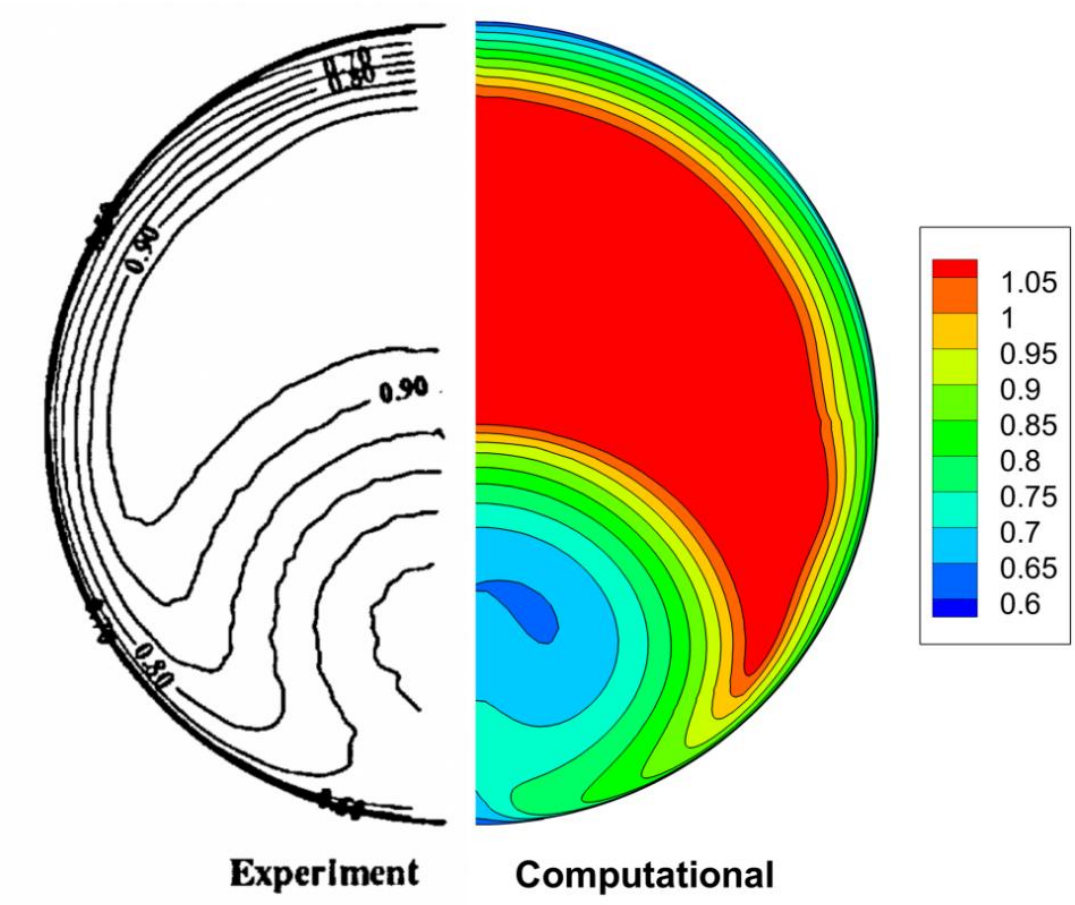

Figure 4.21 Experimental and computed total pressure coefficient contours in AIP.

The presence of secondary flow is also evident in AIP. Secondary flow arises due to curvature of the duct and gives rise to the transverse velocity components which form the counter-rotating vortices. In order to see these vortices, transverse velocity streamlines were plotted in AIP. Figure 4.21 shows the counter-rotating vortices well, in the background are the Mach number contours in color.

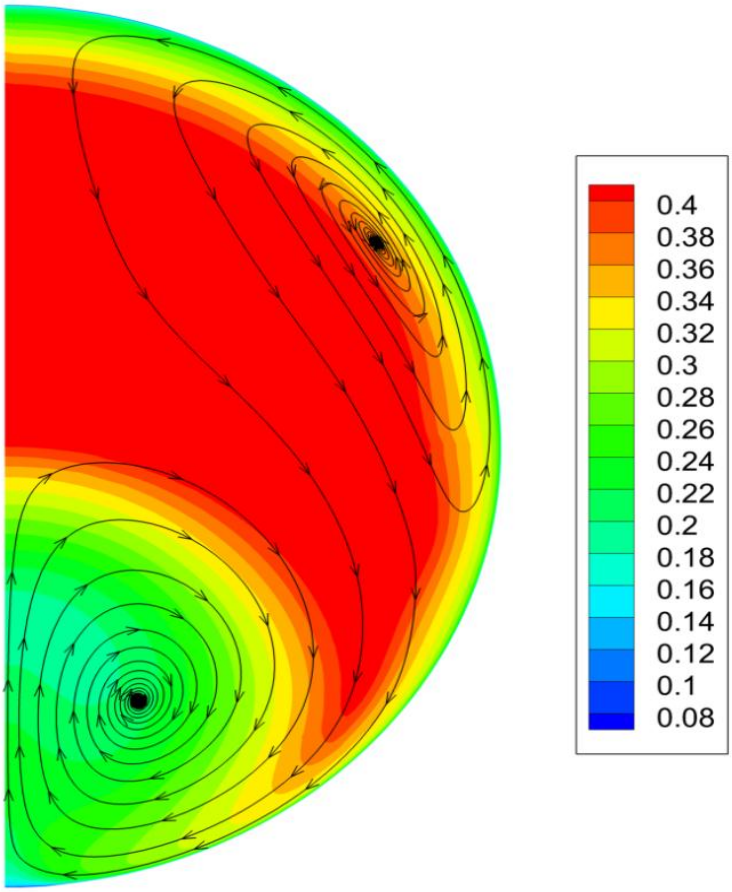

Figure 4.22 Computed secondary flow streamlines in AIP.

Chapter 5

Numerical Simulation of AIAA Propulsion Aerodynamics Workshop S-Duct

The results of the numerical simulation of compressible flow in the AIAA PAW S-Duct are presented in this chapter. The AIAA PAW S-duct is an experimental geometry provided to the propulsion CFD community to present and compare the results of their computations in order to determine best practices for accurate and efficient CFD simulations. The experimental data is not provided but will be provided at the time of workshop. Therefore we present the results of numerical simulations only in this chapter.

5.1 AIAA PAW S-Duct

As mentioned before in Chapter 2, AIAA PAW S-duct is geometrically similar to that in of NASA Glenn S-duct; it is simply a scaled down version of NASA Glenn S-duct. Although the geometry of the AIAA PAW S-Duct is geometrically similar, scaled down version of NASA Glenn S-duct, there are some important differences in the experimental set up in the two cases. The first difference is the way the flow at the inlet of the duct is introduced in the two cases. The inlet flow in the AIAA PAW S-duct is sucked from a bell-mouth open to the atmosphere which is included in the

computational domain as was shown in Figures 2.3 and 2.7. The differences in the inlet flow create a different boundary layer in the developing flow part of the duct, which affects the flow field downstream, especially in the separated flow region. It also affects the secondary flow. The second difference is the inclusion of a mass flow plug in the computational domain as was shown in Figures 2.3 and 2.6. The inclusion of the mass flow plug affects the static pressure distribution and the velocity field as well throughout the duct.

5.2 Results of Numerical Simulation for AIAA Propulsion Aerodynamics Workshop S-Duct

The numerical simulations for the NASA Glenn S-Duct have provided valuable information and insight for simulation and analysis of the AIAA PAW S-Duct flow field. Based on the results in Chapter 4, the k-ω SST turbulence model has been selected for the simulation of the flow field of AIAA PAW S-duct since it provides most accurate and efficient results. Transition SST model was not chosen because it requires the solution of four transport equations making it inefficient compared to the k-ω SST model although it is most accurate among the four models considered in Chapter 4.

Based on the information on AIAA PAW website [8], flow conditions in the simulations were matched both at the outlet and inlet. The air is drawn into the S-Duct at atmospheric conditions; therefore the total pressure and total temperature were set at 101,325 Pa and 293.15 K respectively. The outlet mass flow rate was set at 1.2135 kg/s with a total pressure and total temperature of 88,744 Pa and 286.2 K respectively. Because of significant temperature drop between inlet and exit locations, dynamic viscosity was modeled using the Sunderland's law which relates viscosity to temperature.

The experiments for AIAA PAW s-duct were conducted by ONERA using the 'Kulite 40' dynamic rake as was shown in Figure 1.4. In ONERA experiment, static pressures were measured by the pressure taps located at ϕ=0°, 90º, 180°, and 270º angular locations. Considering again a half model in simulations, the static pressure coefficients are computed at ϕ=0°, 90º, 180° locations in the computations. The AIAA PAW S-duct static pressure coefficients are also compared with those from NASA Glenn experiments because of the geometric symmetry of the two configurations. AIAA PAW website indicates that the static pressure distribution on the lower part of the duct (ϕ=180°) shows region of flow separation from x = 0.23 m to x = 0.25 m.

For this case, boundary layer velocity profile data in the duct inlet plane was not available to compare with the computed velocity profile. Therefore, in Figure 5.1, we have compared the computed velocity profile with the experimental profile of the NASA Glenn S-Duct case. Figure 5.1 shows the turbulent boundary layer velocity profile in non-dimensional parameters discussed before. These parameters, u+ and y+, were calculated using Equations 4.1-4.3 using the computational data of the AIAA PAW case. As expected, the computed boundary layer velocity profile is similar to that in the experiment of NASA S-duct case.

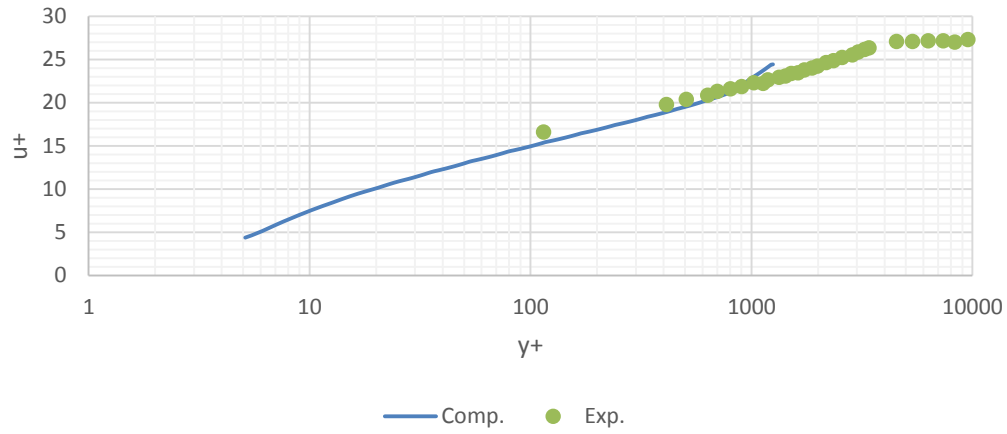

Figure 5.1 Comparison of computed and experimental non-dimensional boundary layer velocity profile, experimental data is from NASA Glenn test.

Figure 5.2 compares the NASA Glenn S-duct computational results with the AIAA PAW S-duct. The static pressure coefficients at each angular location compare well with each other except beyond the exit regions of the ducts. This is due to the difference in the geometries beyond the exit. For the AIAA PAW case, the duct expands rapidly, thus lowering the static pressure rapidly as shown in Figure 5.2 at s/D1=5.73. Since the experimental data for AIAA PAW S-duct is not available for comparison, the comparisons with simulations for NASA S-duct are gratifying in creating confidence in the simulation results for AIAA PAW S-duct.

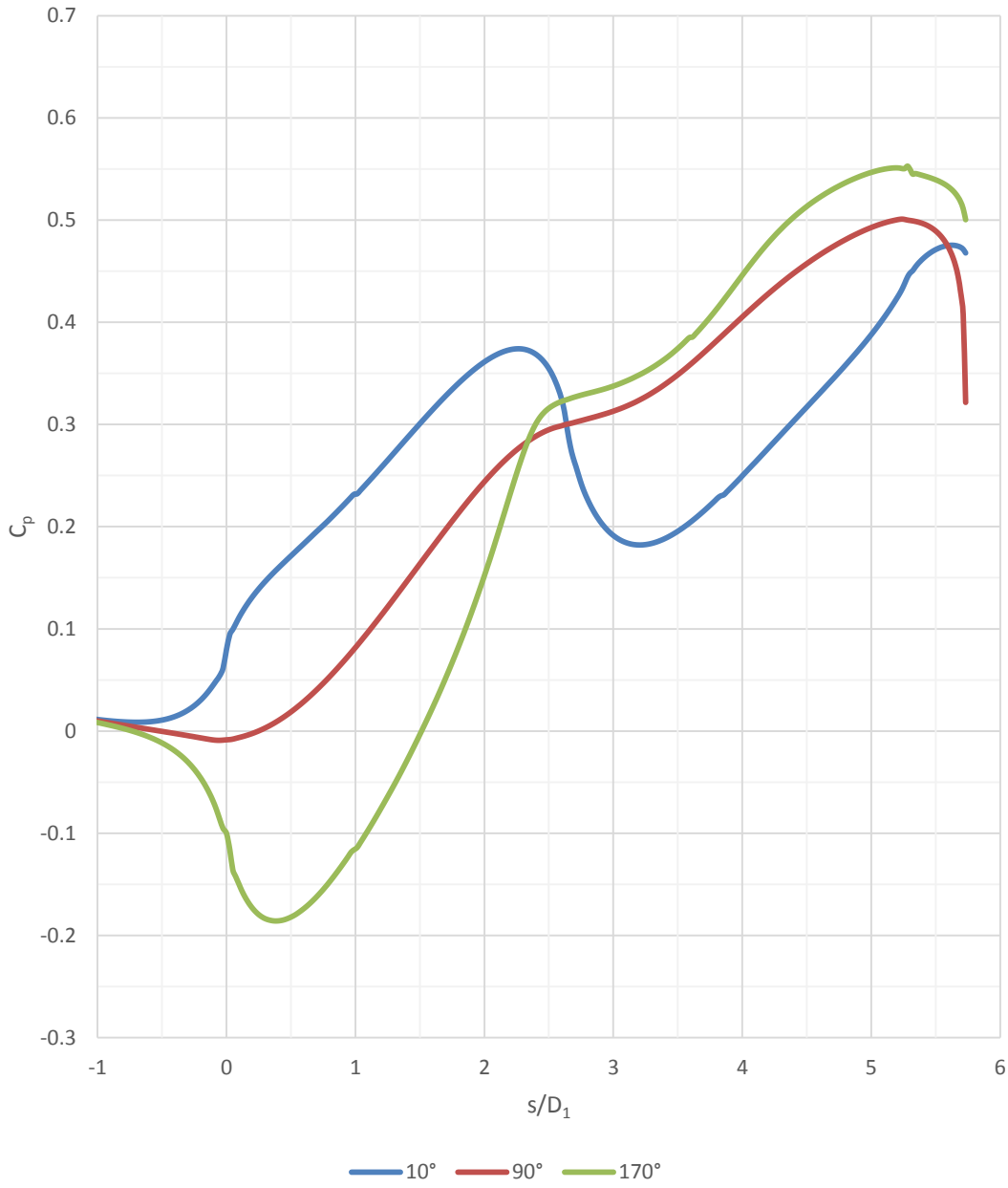

Figure 5.2 Computed static pressure coefficients in compressible flow with k-ω SST turbulence model along the AIAA PAW S-duct at three angular locations: ϕ=10˚, ϕ=90˚ and ϕ=170˚ (they are quite similar to those obtained for the NASA Glenn S-duct in Chapter 4)

Although the experimental results are not available, in order to compare the simulation results with the AIAA PAW S-duct experimental results when they become available,

the computed static pressure coefficient have been plotted at ϕ=0°, 90º, 180° locations corresponding to the locations in the experimental test; these are given in Figure 5.3. In order to determine the separated flow region, static pressure coefficient was plotted against the longitudinal coordinate x as shown in Figure 5.4. From Figure 5.4, it is difficult to ascertain a clear distinct point of separation since the static pressure coefficients at ϕ= 90º and ϕ= 180° locations never truly become constant; their slope becomes very small from x = 0.33 m to x = 0.37 m indicating separation, however these locations are far from the experimental separation point.

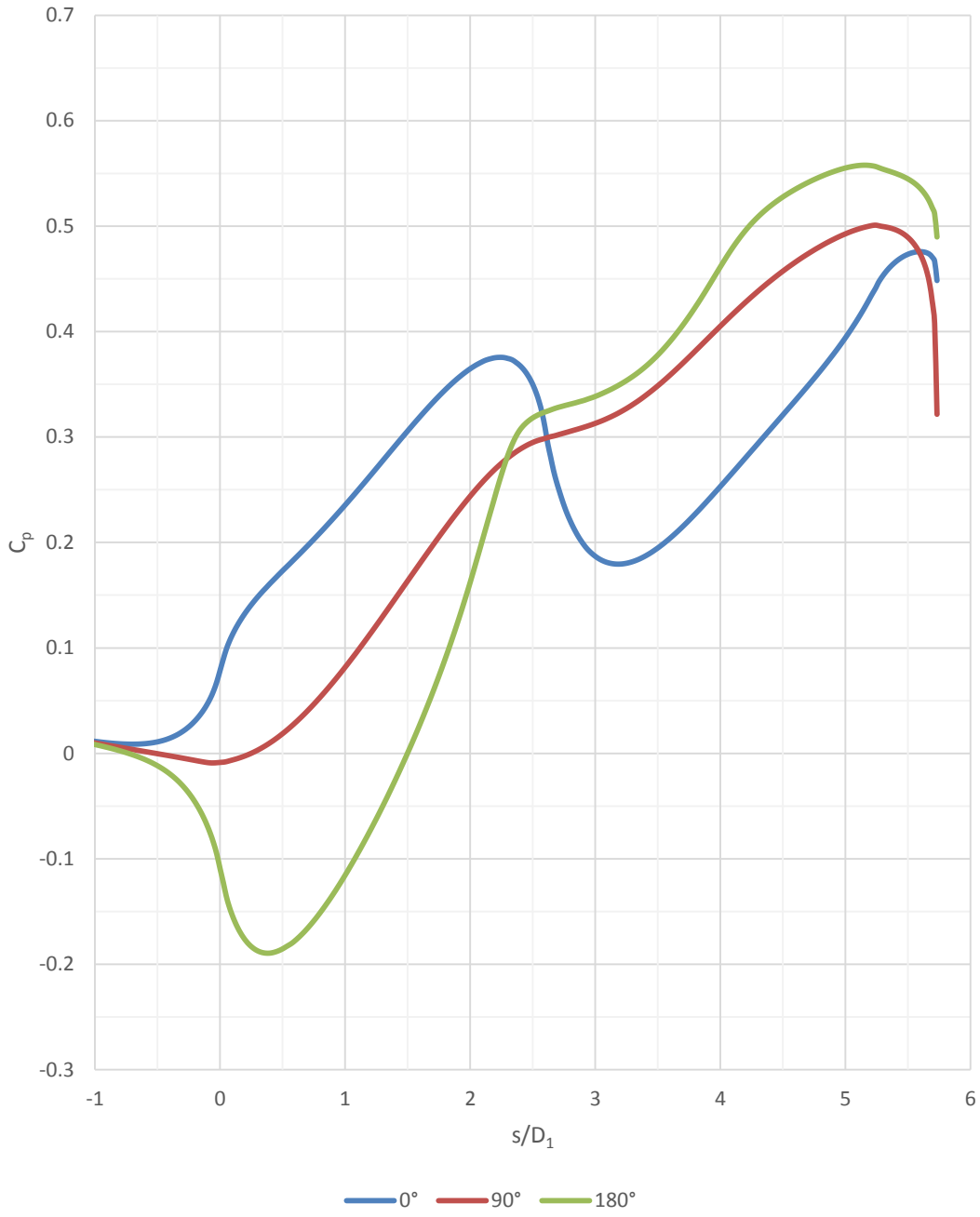

Figure 5.3 Computed static pressure coefficients in compressible flow with k-ω SST turbulence model along the AIAA PAW S-duct at the experimentally defined duct-section at three angular locations: ϕ=10˚, ϕ=90˚ and ϕ=170˚

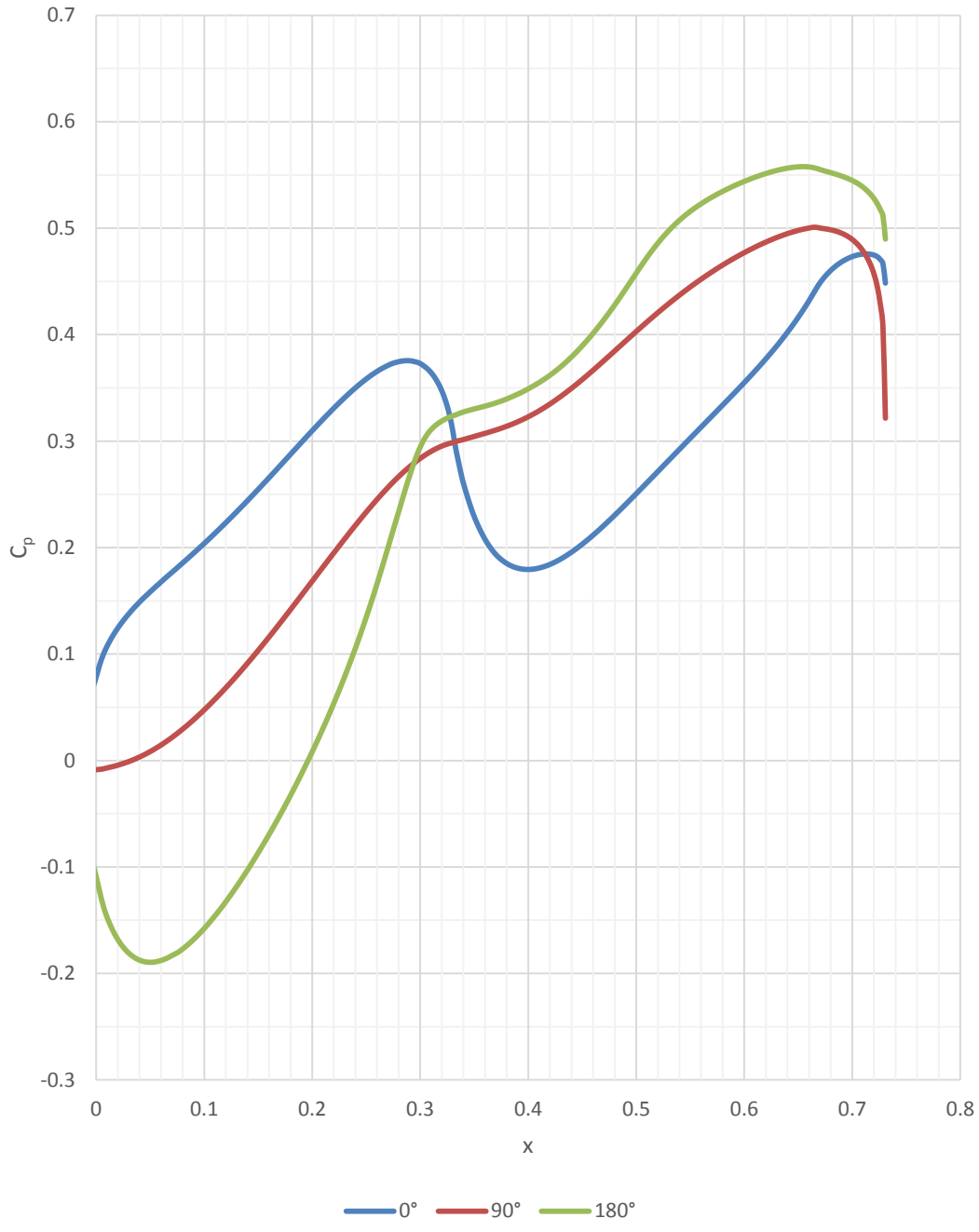

Figure 5.4 Computed static pressure coefficients in compressible flow with k-ω SST turbulence model along the AIAA PAW S-duct at the experimentally defined duct-section at three angular locations: ϕ=10˚, ϕ=90˚ and ϕ=170˚; the pressure is plotted against coordinate x and not s/D_1

Due to this disagreement between the computed and experimentally reported separation location, additional computational investigations of the flow field were conducted. Figure 5.5 shows the velocity vectors in the symmetry plane located at $\phi = 180^{\circ}$. Figure 5.5 shows that the velocity vector at the first grid point off the wall switches direction at x=0.2655 m, which is indicative of the boundary layer separation point. This is within the range of the experimentally reported separation region from x = 0.23 m to x=0.25 m. The late separation predicted by CFD is for this case is similar to the case for the NASA Glenn case reported in Chapter 4.

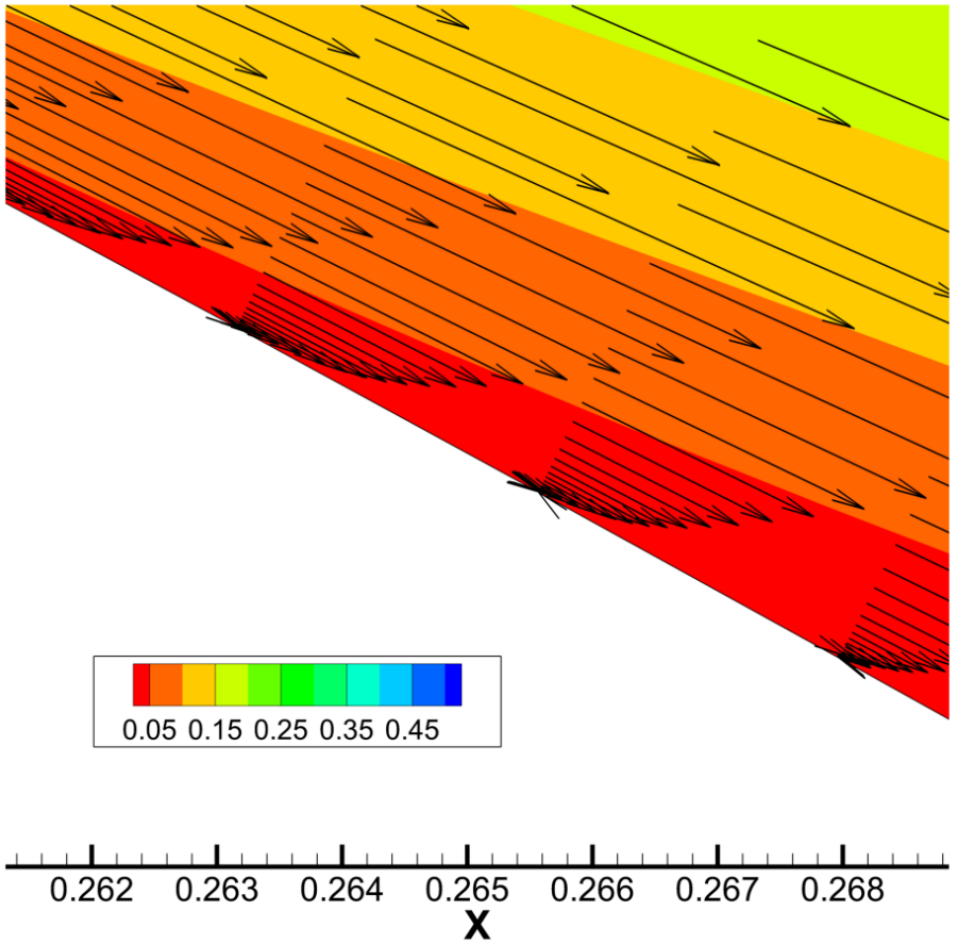

Figure 5.5 Velocity vectors plotted in the plane of symmetry of the duct showing boundary layer separation close to the bottom part of the wall

The differences in the computational domain for the AIAA PAW case result in different flow field patterns in the inlet and exit regions. The bell-mouth inlet is open to the atmosphere, therefore the air is ingested from all around into the bell-mouth. Figure 5.6 shows the velocity streamlines coming into the bell mouth region and entering the S-duct. Figure 5.7 shows the Mach number contours at the reference inlet which still corresponds to s/D1=-0.5. The uniform Mach contours suggest a fully developed flow with a smaller boundary layer thickness. Again the mass flow at the outlet is matched.

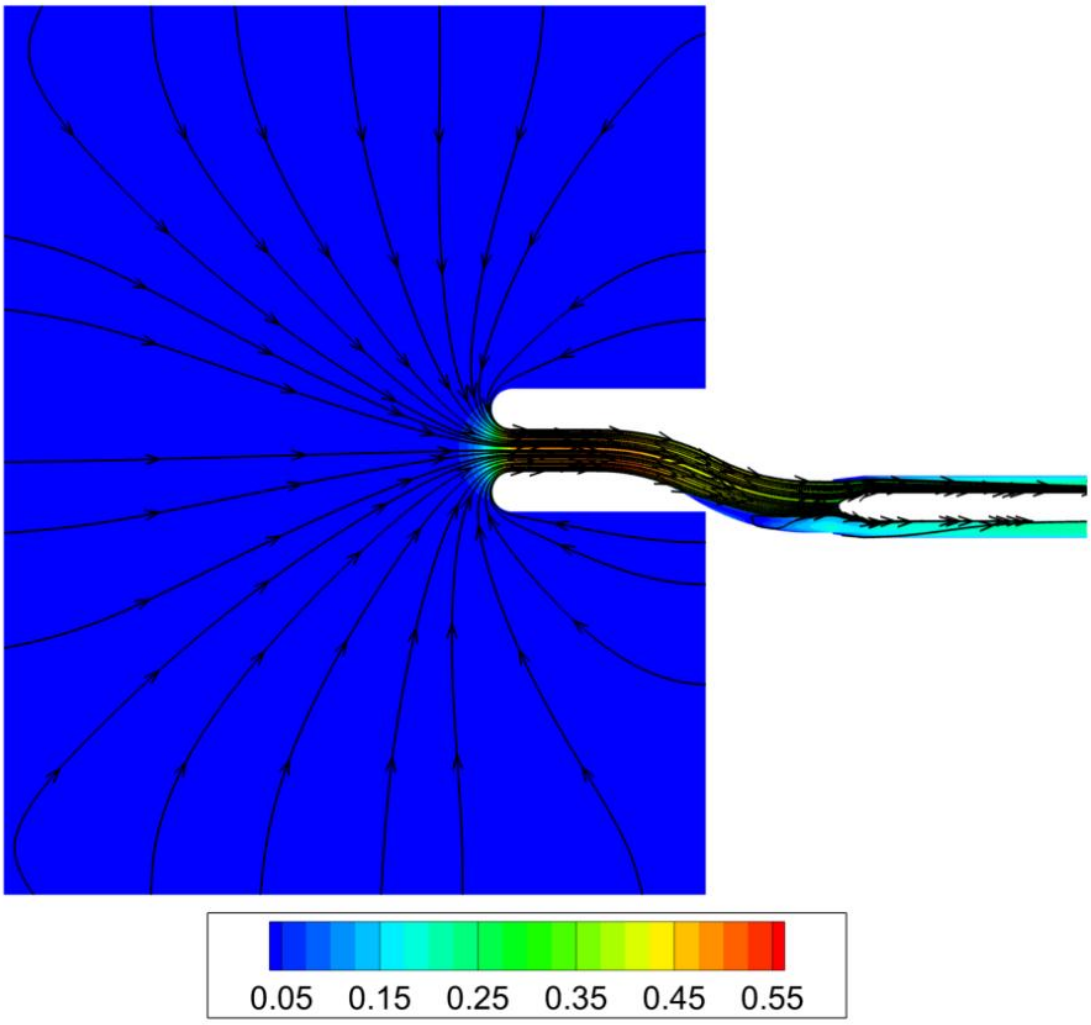

Figure 5.6 Computed streamlines from bell-mouth inlet to the entrance of AIAA PAW S-duct

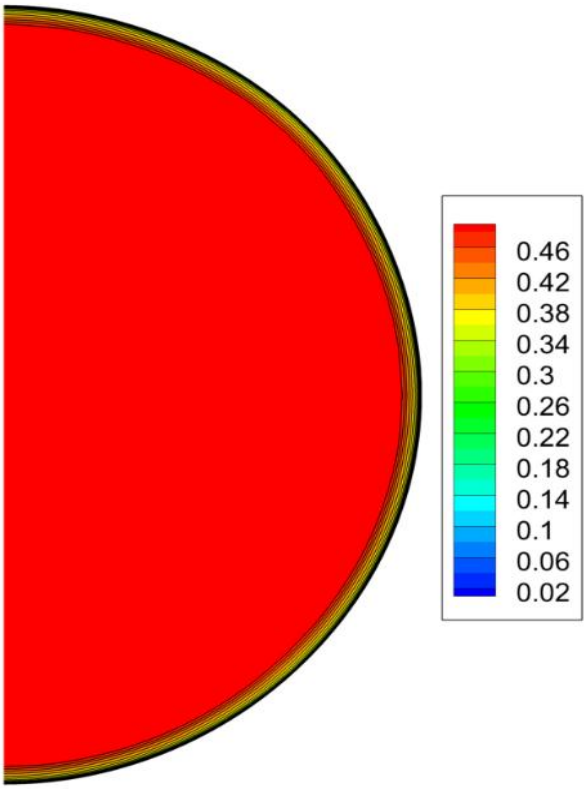

Figure 5.7 Mach number contours at the reference inlet plane of AIAA PAW S-duct

Inclusion of the mass flow plug in the computational domain, close to the AIP causes differences in the flow pattern at the exit of the S-Duct when compared to the NASA Glenn case. Figure 5.8 shows the streamlines along the symmetry plane with Mach number contours. Examining Figure 5.8 and Figure 4.15, it is clear that the height of the separation 'bubble' for the AIAA PAW case compared to that for NASA Glenn case. For a better view of the stream-lines, Figure 5.9 is plotted with inverse contour colors. The stagnation point near the plug creates a high pressure region surrounding the tip as well as slowing of the velocity. Figure 5.10 shows the static pressure contours around the mass flow plug tip, with the highest being in red and lowest in green color. Figure 5.11 shows the Mach number contours around the mass flow tip indicating the slower velocity region.

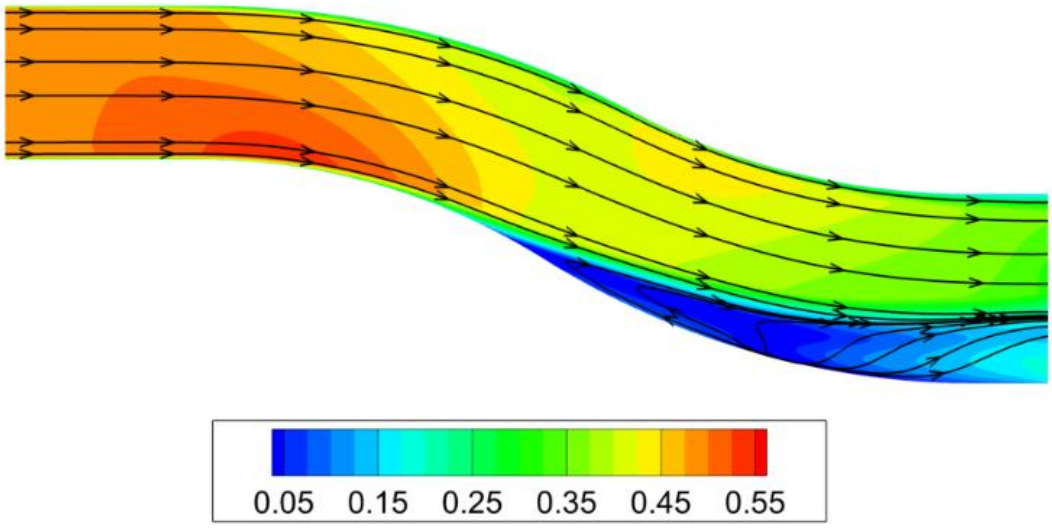

Figure 5.8 Computed streamlines in the AIAA PAW S-duct in the plane of symmetry

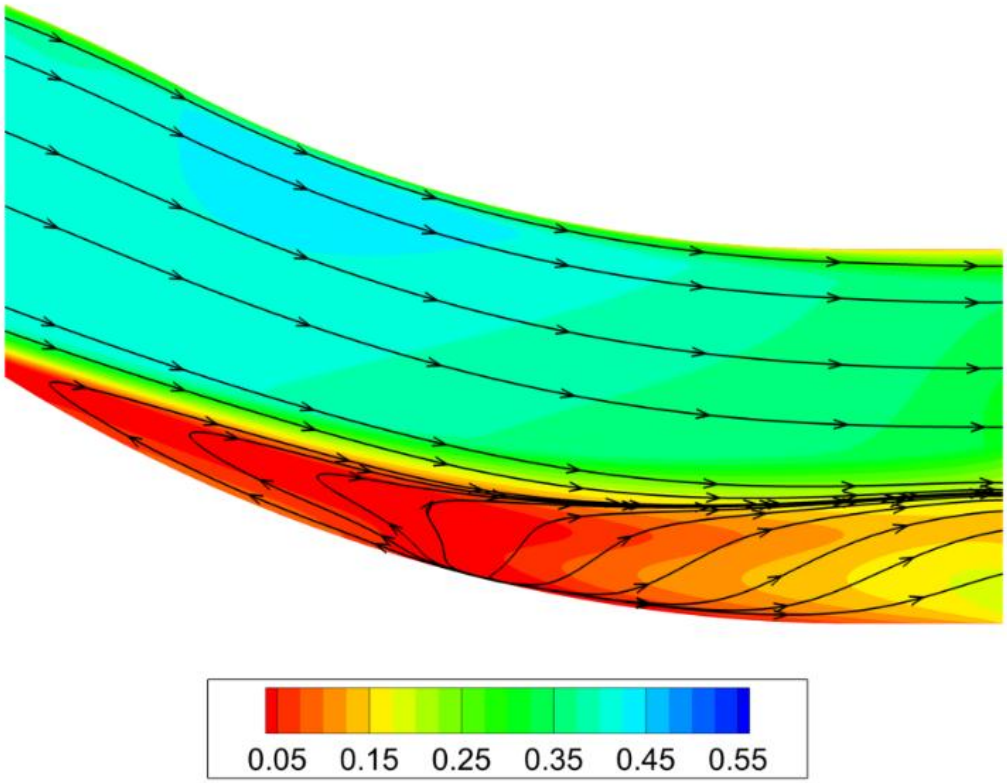

Figure 5.9 Zoomed-in-view of streamlines in plane of symmetry of AIAA PAW S-duct with inverted contour colors

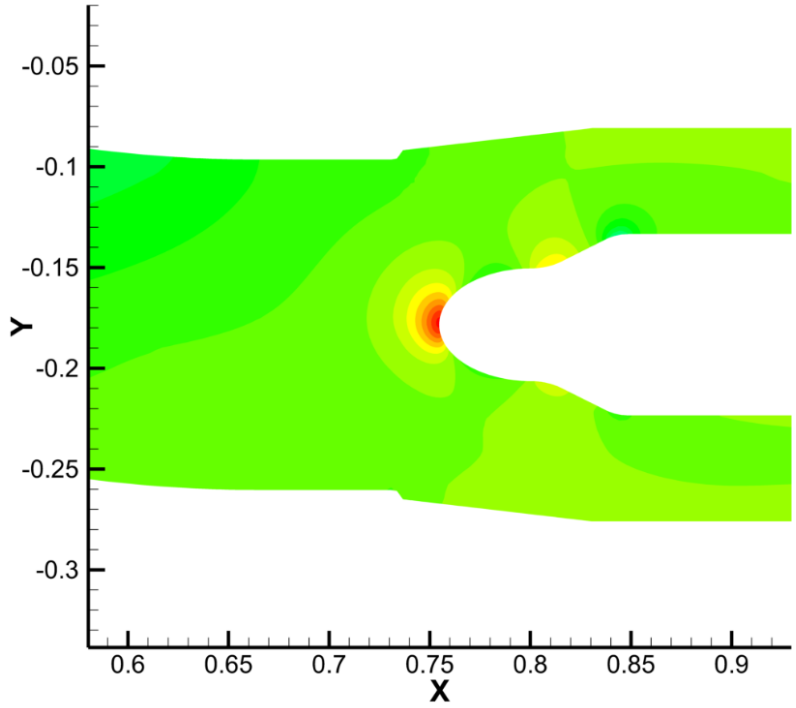

Figure 5.10 Static pressure contours in plane of symmetry at mass flow plug

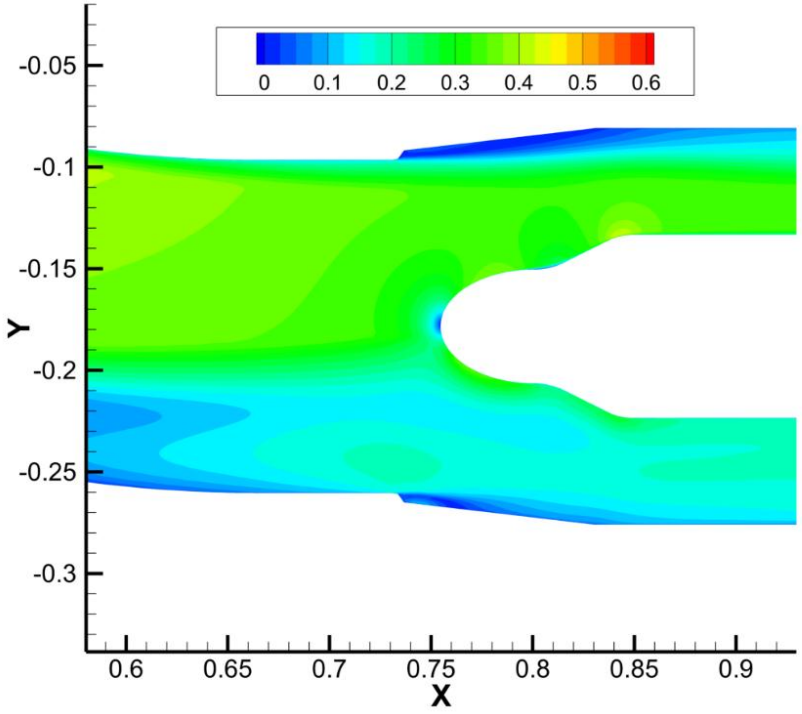

Figure 5.11 Mach number contours in plane of symmetry at mass flow plug

Mach number and static pressure contours at AIP for AIAA PAW S-duct are also different than those in the NASA Glenn case. Figure 5.12 shows the Mach number contours at the AIP. This figure shows the low velocity region near the bottom portion of the duct similar to that in NASA Glenn case, but they also show a lower velocity caused by the mass flow plug at the top of the duct. The slow velocity region caused by the mass flow plug is indicated by the semi-circular contours of lower Mach numbers.

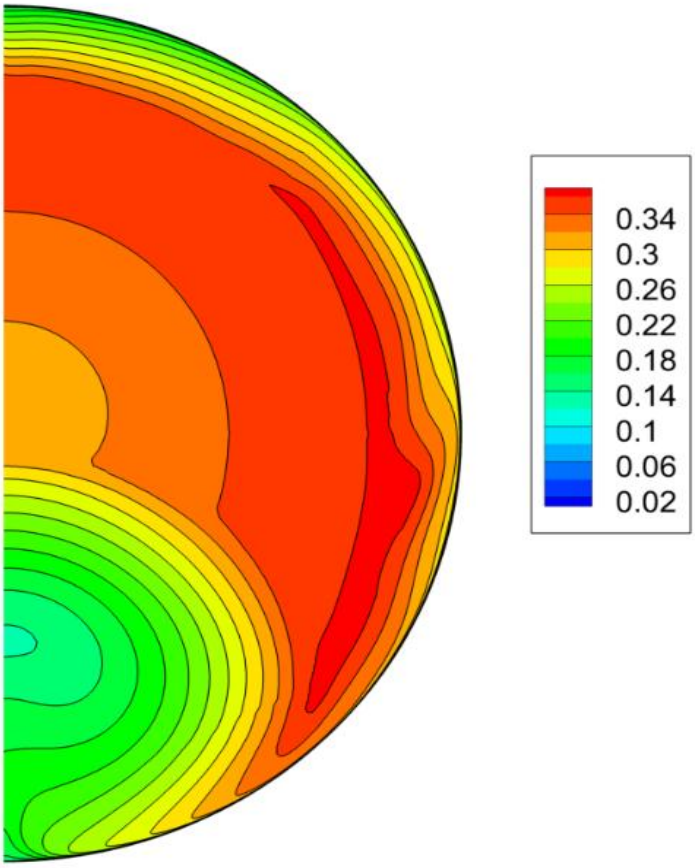

Figure 5.12 Mach number contours at AIP in AIAA PAW S-duct

Total pressure coefficient contours have a similar shape to that in the NASA Glenn case reported in Chapter 4. Figure 5.13 shows the total pressure contours at the AIP in the AIAA PAW case. These contours are much lower in value than those in the NASA

Glenn case. The high pressure region caused by the mass flow plug is not apparent in these contours.

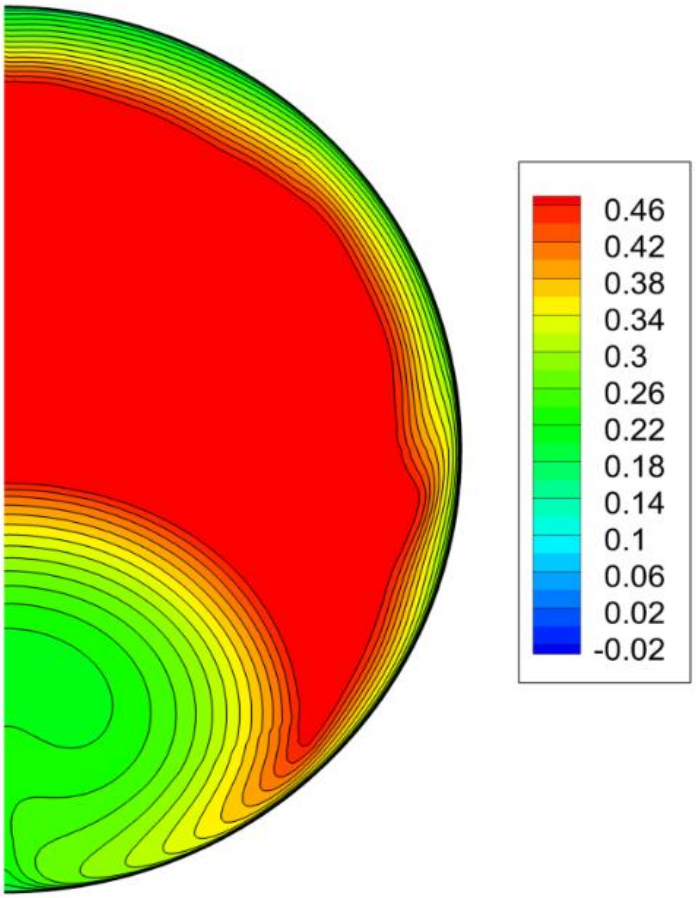

Figure 5.13 Total pressure coefficient contours at AIP in AIAA PAW S-duct

Transverse velocity streamlines are very different in the AIAA PAW case compared to those in the NASA Glenn case. These streamlines, as shown in Figure 5.14, show the secondary flow and a counter rotating vortex in the lower portion of the duct. The mass flow plug contributes to this flow behavior by restricting and routing the flow through the later part of duct.

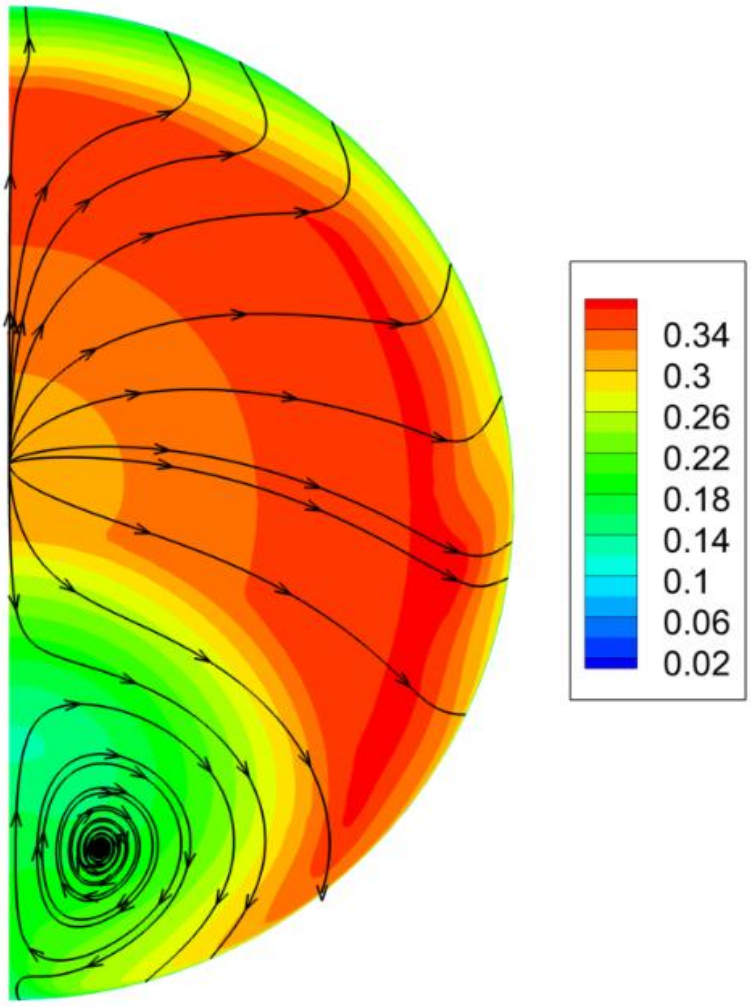

Figure 5.14 Transverse velocity streamlines at AIP for AIAA PAW S-Duct

The results of the numerical simulation of compressible flow using a two-equation k-ω SST model for the AIAA PAW S-Duct are presented in this chapter. The AIAA PAW has provided an experimental geometry for simulation by the CFD researchers in order to establish best practices for accurate and efficient CFD simulations for this benchmark test case. The experimental results will be provided at a later date at the time of the workshop.

Chapter 6

Conclusions and Future Research

This chapter summarizes the results of this study and provides some directions for future research.

6.1 Conclusions

In this thesis, numerical simulations of two S-duct flow fields have been conducted. The first simulation case corresponds to the experimental study conducted at NASA Glenn Research Center in early 1990s. The second simulation study corresponds to the S-duct case proposed in AIAA Propulsion Aerodynamics Workshop (PAW) for which experimented have been conducted at ONERA in France (the experimental data has not been released at this time). Flow inside an S-Duct is characterized by a small region of separation and secondary flow. CFD software ANSYS-FLUENT was employed on a computational structured mesh for solving the Reynolds-Averaged Navier-Stokes (RANS) equations in conjunction with four different turbulence models – one-equation Spalart-Allmaras (SA) model, two-equation k - ε and k – ω SST models and the four equation Transition SST model. Multiple turbulence models to evaluate their impact on the accuracy of the results. Among the four turbulence models, Transition SST models predicted the best results comparing with the NASA Glenn experimental data for the static pressure coefficient, however it is computationally less efficient because it requires the solution of four transport equations. The results from k-ω SST turbulence model were very close to those predicted by Transition SST model but it is twice more efficient because it requires the solution of only two transport equations. Therefore it

was employed in the AIAA PAW S-duct study. Both incompressible and compressible form of governing equations was employed to determine the effect of compressibility. It was concluded that at inlet Mach of M = 0.6, the compressibility must be included in the simulations. The study has been able to establish the best practice guidelines in terms of the requirements of suitable mesh density and density based second-order algorithm for the solution of compressible Reynolds-Averaged Navier-Stokes equations with a two-equation k-ω SST turbulence model to obtain the accurate and efficient CFD solutions.

6.2 Future Research

There are several aspects of simulations where future research efforts should be directed. Large-Eddy-Simulation (LES) and Detached-Eddy-Simulation (DES) models should be employed for including the effects of turbulence; they are likely to improve the results. Simulations with both passive and active flow control devices should be conducted to remove the separation bubble and increase the flow uniformity at AIP and improve the pressure recovery [7]. In addition, flow field simulations from slightly bent ducts to highly curved and bent ducts should be conducted to evaluate their effectiveness for various applications. In addition, transient analysis of the flow field should be conducted to analyze the problem of inlet flow start/unstart.

Appendix A

User Defined Function to Calculate the Mach Number for Incompressible Flow Model

```
/************************************************************************
UDF to calculate mach number field function and store in
user-defined memory. .
************************************************************************/
#include "udf.h"
DEFINE_ON_DEMAND(Mach_Number)
{
Domain *d; /* declare domain pointer since it is not passed as an
argument to the DEFINE macro */
real a = 347.4;

Thread *t;
cell_t c;
d = Get_Domain(1); /* Get the domain using Fluent utility */
/* Loop over all cell threads in the domain */
thread_loop_c(t,d)
{
/* Compute temperature function and store in user-defined memory*/
```

```
/*(location index 0) */
begin_c_loop(c,t)
{

C_UDMI(c,t,0) = sqrt(SQR(C_U(c,t))+SQR(C_V(c,t))+SQR(C_W(c,t)))/a;

}
end_c_loop(c,t)
}
}
```

Appendix B

User Defined Function to Calculate Total Pressure Coefficient

```
/**********************************************************************
UDF to calculate speed of sound from varying density, Mach number from varying speed of sound, and total pressure for total pressure
coefficient calculation
**********************************************************************/
#include "udf.h"
#include "math.h"
DEFINE_ON_DEMAND(Mach_Number)
{
Domain *d; /* declare domain pointer since it is not passed as an
argument to the DEFINE macro */
real a=347.4;
real pclo=113212.5943;
real pcl=90144.34941;
real gamma=1.4;

Thread *t;
cell_t c;
d = Get_Domain(1); /* Get the domain using Fluent utility */
/* Loop over all cell threads in the domain */
```

```
thread_loop_c(t,d)
{
/* Compute temperature function and store in user-defined memory*/
/*(location index 0) */
begin_c_loop(c,t)
{

        /* Finds Speed of Sound Based on pressure and Density */
C_UDMI(c,t,0) = sqrt(gamma*(C_P(c,t)/C_R(c,t)));
        /* Finds Mach number based on speed of sound */
C_UDMI(c,t,1)                                                                    =
sqrt(SQR(C_U(c,t))+SQR(C_V(c,t))+SQR(C_W(c,t)))/C_UDMI(c,t,0);
        /* Finds total pressure based off speed of sound */
C_UDMI(c,t,2)                  =                C_P(c,t)*pow((1+((gamma-
1)/2)*SQR(C_UDMI(c,t,1))),(gamma/(gamma-1)));
        /* Finds total pressure coefficient */
C_UDMI(c,t,3) = (C_UDMI(c,t,2)-pcl)/(pclo-pcl);

}
end_c_loop(c,t)
}
}
```

References

[1] Wellborn, S.R., Okiishi, T.H., and Reichert, B.A, "A Study of Compressible Flow through a Diffusing S-Duct," NASA Technical Memorandum 106411, December 1993.

[2] http://l1011project.blogspot.com/2011/06/l-1011-general-aircraft-characteristics_04.html

[3] Wellborn, S.R., Reichert, B.A, and Okiishi, T.H., "An Experimental Investigation of the Flow in a Diffusing S-Duct," AIAA-92-3622, 28th Joint Propulsion Conference and Exhibit, Nashville, TN, 6-8 July 1992.

[4] Harloff, G.J., Reichert, B.A, and Wellborn, S.R., "Navier-Stokes Analysis and Experimental Data Comparison of Compressible Flow in a Diffusing S-Duct," AIAA-92-2699, 10th Applied Aerodynamics Conference Exhibit, Palo Alto, CA, June 22-24, 1992.

[5] Vuillerme, A.L., Deck, S., and Chevrier, R., "Numerical Simulation of the Flow Inside an S-Shaped Intake Diffuser," European Conference for Aerospace Sciences, Moscow, Russia, July 4-7, 2005.

[6] Garnier, E., Leplat, M., Monnier, J.C., and Delva, J., "Flow Control by Pulsed Jet in a Highly Bended S-Duct," AIAA Paper 2012-3250, AIAA 6th Flow Control Conference, New Orleans, LA, 25-28 June 2012.

[7] www.aiaa.tecplot.com

[8] ANSYS ICEM CFD 13: Geometry and Mesh Generation Preprocessor, Ansys Inc., 2012.

[9] ANSYS Fluent 13: Flow Modeling Software, Ansys Inc., 2012.

Vita

Colin J. Fiola

Degrees M.S. Aerospace Engineering, Augus 2013
B.S. Mechanical Engineering, May 2008

Professional Societies American Institute of Aeronautics and Astronautics

Colin is currently working as a Lead Engineer / Technologist for GE Aviation's Thermal Systems Design section.

Aug. 2013